Society for Science and Education
United Kingdom

ISSN: 2055 - 1266
Volume 1. Issue 6

Journal of Biomedical Engineering and Medical Imaging

TABLE OF CONTENTS

EDITORIAL ADVISORY BOARD

DISCLAIMER

All the contributions are published in good faith and intentions to promote and encourage research activities around the globe. The contributions are property of their respective authors/owners and the journal is not responsible for any content that hurts someone's views or feelings etc.

SOCIETY FOR SCIENCE AND EDUCATION
UNITED KINGDOM

JBEMi JOURNAL OF BIOMEDICAL ENGINEERING AND MEDICAL IMAGING

ISSN: 2055-1266
VOLUME 1, ISSUE 6

A Novel Segmentation and Contouring Scheme to Assist Accurate Brain Lesion Classification

[1]Madhukumar, S. and [2]N.Santhiyakumari
[1]Department of Electronics and Communication Engineering,
St Joseph's College of Engineering and Technology, Palai, Kottayam, India
[2]Department of Electronics and Communication Engineering,
Knowledge Institute of Technology, Salem, India
[1]madlekarthi@gmail.com, [2]santhiyarajee@rediffmail.com

ABSTRACT

Segmentation of highly infiltrating glioblastoma multiforme (GBM) in BrainMR Images has been highly challenging as the grey levels of tumor and peritumoral vasogenic edema are quite homogenous and hence identifying a suitable scheme for isolating GBM from the background has been troublesome.This paper proposes a novel segmentation and contouring scheme, using shape sensitive derivative strategy for segmentation and energy minimizing contours for enhancing the edges of the GBM, under investigation. The efficiency of the algorithm has been tested with the aid of extracted tumor features, the Shape Features -circularity, irregularity, Area, Perimeter, Shape Index, Intensity features – Mean, Variance, Standard Variance, Median Intensity, Skewness, and Kurtosis, Texture features –Contrast, Correlation, Entropy, Energy, Homogeneity, cluster shade, sum of square variance. It is obvious, though this algorithm consumes more computational time, it segments the edges effectively and preserve the shape facilitating accurate extraction or estimation of the features further and provides stable and reproducible results. All the classification Schemes, with combined DA and SVM with Higher Rank Features and LDA techniques exhibited appreciable improvement in terms of sensitivity, specificity, positive Predictive value and negative Predictive value, because of the accuracy of shape sensitive derivative segmentation algorithm and energy minimizing contour algorithm.

Keywords: Magnetic Resonance Brain images, class separable shape sensitive segmentation, Energy Minimizing Contours, Image Enhancement.

1 Introduction

Segmentation of Brain structures, for estimation of various parameters, is one of the primary steps, towards the design of efficient image based Clinical Decision Support Systems (CDSS). The main aim of segmentation in CDSS is to recognise homogeneous regions within an image as distinct features and enable them to be classified as different objects. [1] The segmentation process can be based on finding the maximum homogeneity in grey levels within the regions identified. One of the common problems encountered in image segmentation is choosing a suitable approach for isolating different objects from the background. [2] The segmentation does not perform well if the grey levels of different objects are

DOI: 10.14738/jbemi.16.546
Publication Date: 17th November 2014
URL: http://dx.doi.org/10.14738/jbemi.16.546

quite similar as in the case of B mode Magnetic Resonance. The presence of speckling artefacts further increases the complexity of the system. It is expected that an ideal segmentation scheme will enhance the boundary differences between the objects and their background making the parameter estimation task easier and accurate. [3] Other issues related to segmentation involve choosing good segmentation algorithm, measuring their performance, and understanding their impact on the scene analysis system. Classical image segmentation techniques are based on two pixel characteristics: discontinuities and similarities. Discontinuity is an approach to partition the image based on abrupt changes in intensity (or) gray level. Similarity is an approach based on partitioning an image into regions according to a set of pre-defined criteria. [4] Many of the classical techniques like Region growing, a procedure that groups pixels (or) sub regions into larger regions have been applied to try to solve this problem with variable outcomes. Such techniques tend to be unreliable when segmenting a structure that is surrounded by others with similar image intensity (e.g., low-contrast structures). More sophisticated techniques, like level set method (LSM) is a numerical technique for tracking interfaces and shapes. The advantage of the level set method is that one can perform numerical computations involving curves and surfaces on a fixed Cartesian grid without having to parameterize these objects), use more powerful computations for tracking the evolution of moving surface. [5] An initial approximation of the solution evolves until it gets the limits of the region of interest. In this paper, the shape sensitive derivative approach which quantifies the sensitivity of the problem when the domain under consideration is perturbed by changing the material property at a specific point has been utilized. The problem of segmentation of Magnetic Resonance images has been achieved via optimization of a cost function by asymptotic expansion. Optimal shape estimation plays a vital role in feature estimation and pattern recognition techniques. The segmented images are contoured using energy minimizing contours. This novel scheme has been tested on Brain images for estimating the features for providing enhanced Obstetric care. Experiments were carried out with first, second and third trimester Brain images and found to produce stable and reproducible results.

2 Derivative Based Image Segmentation Algorithm

Feature segmentation of Magnetic Resonance images is a multi-disciplinary challenge including expertise in signal and image processing, optimization theory and requires a detailed anatomical knowledge of the subject under study. Wide variety of segmentation schemes can be found in the literature and these can be broadly categorized as Boundary-based, Region based, Shape Model approaches and thresholding schemes. Boundary based algorithms extract the region of interest based upon the intensity variation at the edges as they expect the ROI to have some perfect demarcation at the edges. These algorithms can further be grouped into optimum boundary based schemes; active contours based algorithms and level sets [6]. Another group of segmentation schemes are the region based methods which extract the region of interest based on the similarity measure. A seed pixel is initialized first and the predefined similarity measure is used to evaluate the degree of similarity between the pixels. A number of region based schemes are present in the literatures which are based on clustering, graph cut, fuzzy connectedness, MRF, watersheds and optimum partitioning (Mumford-Shah, Chan-Vese). Another classification of the segmentation algorithms are the Shape Model approaches [2] [7]. These algorithms play a vital role in real time applications are focused much in the recent years by researchers. They tend to extract out the features based upon the prior knowledge of the shape of the

feature to be extracted. Some of the Shape based approaches cited in the literature are manual tracing methods, Live wire techniques, Active Shape and Active Appearance approaches and atlas-based methods [8] [9] [10].

The introduction of the Topological Derivative allows to quantify the sensitivity of cost function when domain under consideration is perturbed, and it indicates the best place where perturbation could be introduced. The topological shape sensitive derivative is computed for an appropriate functional associated to the image indicating the cost endowed to specific image segmentation [8].

The image segmentation algorithm based on this derivative can be proposed as follows. Let $\mathcal{J}(\Omega) = \mathcal{J}(\phi(\Omega))$ be the cost function to be minimized and $\phi(\Omega)$ the solution of an associated variational problem (VP) defined in the domain (Ω). For a small parameter $\epsilon \geq 0$, let Ω_ϵ be the perturbed domain obtained by the insertion of heterogeneity on the parameters governing the associated VP. This heterogeneity has been defined in a small ball of radius ϵ centred at any point $\hat{x}$ of the domain Ω. Furthermore, let ϕ_ϵ be the solution of the VP defined in the perturbed domain Ω_ϵ. Then, for small values of parameter ϵ the topological sensitivity provides an asymptotic expansion of $\mathcal{J}(\Omega_\epsilon)$ (it is a series of functions which has the property of truncating the series after a finite number of terms provided an approximation to a given function).

$$\mathcal{J}(\Omega_\epsilon) = \mathcal{J}(\Omega) + f(\epsilon) D_T(\hat{x}) + o\big(f(\epsilon)\big) \quad (1)$$

Where, $\mathcal{J}(\Omega_\epsilon)$ is the shape derivative of cost function in relation to the parameter ϵ, $f(\epsilon)$ is the positive function going monotonically to zero with ϵ and $D_T(\hat{x})$ is the Topological derivative. This derivative can be seen as a first order correction on $\mathcal{J}(\Omega)$ to estimate $\mathcal{J}(\Omega_\epsilon)$. Since $f(\epsilon)$ is positive, the heterogeneity must be introduced at any point $\hat{x}$ where D_T is negative in order to reduce the value of the cost function $\mathcal{J}$. The topological derivative can be easily obtained and this segmentation method appears robust even in the presence of very large noise in the image data. Initially we present the formulation of the segmentation problem. In particular, we define the cost functional associated to a specific segmentation of the image data. We also define the variational problem (VP) which characterizes function ϕ. The proposed segmentation algorithm and numerical approximation used to find an approximated solution of the associated VP [8].

2.1 Problem Formulation

The image data is normally characterized by a two-dimensional matrix of pixels or a three dimensional matrix of voxels, which is the brightness level or grey level intensity at that point. Thus, to each image element is associated an intensity. The original image data can be described by a real valued functions *v* which is constant at image element level, then,

$$v \in \mathcal{V} = \{w \in L^2(\Omega)\} \quad (2)$$

Where,

$\mathcal{V}$ - Close subspace of domain.
w - Constant at image element level.
L - Limit point of the domain.
Ω - An open bounded domain in $\mathbb{R}^n$, n = 2, 3.

In addition let us define the set as classes *C*,

$$C = \{c_i \in \mathbb{R} : \mathrm{i} = 1, \cdots \mathrm{N_c}\} \tag{3}$$

Where, N_c is the number of predefined classes in which the original image υ will be segmented. c_i -Represents the intensity that characterizes the i^{th} class. The image segmentation problem can be stated as following: Given the image data $\upsilon \in \mathcal{V}$ find the segmented image $u^* \in U$ such that minimizes a functional $\mathcal{J}$: $U \rightarrow \mathbb{R}$ endowed to the cost of a specific segmented image and being *U* defined as,

$$U = \{\mathrm{u} \in \mathcal{V} : u(x) \in C \forall x \in \Omega\} \tag{4}$$

The degree of match between an image and segmentation can be best estimated using Mumford and Shah functional measure. Hence by Mumford and Shah functional, the cost functional *J* associated to a segmented image $u \in U$ can be given by,

$$\mathcal{J}(\Omega) = \frac{1}{2}\int_{\Omega} \mathbb{K}\nabla\varphi.\nabla\varphi d\Omega + \frac{1}{2}\int_{\Omega} (\varphi - (\upsilon - u))^2 \, d\Omega \tag{5}$$

Where field ϕ is solution of the following variational problem: Find $\phi \in \mathrm{H}^1(\Omega)$ such that,

$$a(\varphi, \eta) = l(\eta) \forall \eta \in \mathrm{H}^1(\Omega) \tag{6}$$

With the Bilinear form $a(\cdot, \cdot)$ - $\mathrm{H}^1(\Omega) \times \mathrm{H}^1(\Omega) \rightarrow \mathrm{R}$.

Linear form $l(\cdot)$ - $\mathrm{L}^2(\Omega) \rightarrow \mathrm{R}$.

The bilinear and linear form of the variational problem can be redefined as

$$a(\varphi, \eta) = \int_{\Omega} \mathbb{K}\nabla\varphi.\nabla\eta \, \mathrm{d}\,\Omega + \int_{\Omega} \varphi\eta \, \mathrm{d}\Omega \tag{7}$$

$$l(\eta) = \beta \int_{\Omega} (\upsilon - \mathrm{u})\eta \, \mathrm{d}\Omega \tag{8}$$

Where, β is the parameter chosen experimentally and $\mathbb{K}$ is the diffusivity of second order tensor field which is constant at image element level. The existence and uniqueness of the solution ϕ of the variational problem can be estimated through Lax-Milgram theorem.

Associated to ϕ is defined the function ϕ_ϵ solution of a perturbed variational formulation. The perturbation has been characterized by changing the segmented image *u* with a new one u_T which is identical to *u* at every point of the domain Ω except in the small region B_ϵ centered at point $\hat{x} \in \Omega$.

In B_ϵ, u_T assumes one of the values $c_i \in C$. Formally,

$$u_T(x) = u(x) \forall x \in \Omega \backslash \overline{B\epsilon}$$

$$u_T(x) = c_i . c_i \in C \; \forall x \in B_\epsilon$$

Therefore, the perturbed cost functional becomes

$$\mathcal{J}(\Omega_\epsilon) = \tfrac{1}{2}\int_{\Omega} \mathbb{K}\nabla\varphi_\epsilon . \nabla\varphi_\epsilon d\Omega + \tfrac{1}{2}\int_{\Omega} (\varphi_\epsilon - (\upsilon - u_T))^2 \, d\Omega \tag{9}$$

Where field ϕ_ϵ is solution of the perturbed variational problem: Find $\phi_\epsilon \in H^1(\Omega)$ such that:

$$a(\varphi_\epsilon, \eta) = l_\epsilon(\eta) \quad \forall \eta \in H^1(\Omega) \tag{10}$$

With $l(\cdot) : L^2(\Omega) \rightarrow \mathbb{R}$ defined as:

$$l_\epsilon(\eta) = \beta \int_\Omega (v - u_T)\eta d\Omega \quad (11)$$

Satisfying the same properties established by expressions (9-11). Moreover, from these properties the following estimate holds,

$$\|\varphi_\epsilon - \varphi\|_{H^1(\Omega)} \leq C|B_\epsilon|^{1/2} \quad (12)$$

Where, C is the Constant independent of ϵ and | B_ϵ | is the Lebesgue measure of B_ϵ.

In mathematics, the Lebesgue measure, named after Henri Lebesgue, is the standard way of assigning a length, area or volume to subsets. It has used throughout real analysis, in particular to define Lebesgue integration. Sets which can be assigned a volume are called Lebesgue measurable, the volume or measure of the Lebesgue measurable set *A* is denoted by λ (*A*). A Lebesgue measure of ∞ is possible, but even so, assuming the axiom of choice, not all subsets of R^n are Lebesgue measurable. Lebesgue measure is often denoted d*x*, but this should not be confused with the distinct notion of a volume form.

2.2 Computation of the Const Function

The topological derivative allows us to quantify the sensitivity of the problem when the domain under consideration is perturbed by introducing a hole, an inclusion or a source term in a small region Bϵ (B_ϵ is a ball of radius ϵ). The topological derivative is given by the following limit (ϵ→0), [11]

$$D_T(\hat{x}) = lim_{\epsilon \to 0} \quad \frac{\mathcal{J}(\Omega_\epsilon) - \mathcal{J}(\Omega)}{f(\epsilon)} \quad (13)$$

Using the Topological-Shape Sensitivity Method, the topological derivative can be also written as:

$$D_T(\hat{x}) = lim_{\epsilon \to 0} \quad \frac{1}{f'(\epsilon)} \frac{d}{d\epsilon} \mathcal{J}(\Omega_\epsilon) \quad (14)$$

Where the derivative of the cost function with respect to the parameter ϵ may be seen as its classical shape derivative. Applying Renold Transport Theorem and simplifying using tensorial equations, the localized cost function for segmentation can be obtained as

$$D_T(\hat{x}) = \tfrac{1}{2}(c_i - u)\left[\left(\varphi(\hat{x}) - (v - u)\right) + \left(\varphi(\hat{x}) - (v - c_i)\right)2(1 - \beta)\varphi(\hat{x})\right] \forall \hat{x} \in \quad (15)$$

The topological derivative at any point $\hat{x} \in \Omega$ only depends on the value at that point of the function ϕ solution of the variational problem given by (6) defined in the non-perturbed domain Ω, on the image data *v*, on the actual segmented image *u* and on the perturbation given by one of the intensity values characterizing the N*c* classes $c_i \in C$ in which the image data *v* will be segmented. Moreover, from (1) and since *f* (ϵ) is positive, by introducing a perturbation at any point $\hat{x}$ where $D_T(\hat{x})$ is negative we will obtain a cutback on the cost function value. Then, D_T can be taken as an indicator function defining the best places where the perturbations could be introduced. Since the solution ϕ of the variational problem given by (23) cannot, in general, be known explicitly an approximate solution is mandatory. To this end the Finite Element Method will be adopted for the numerical experiments to be shown later. The finite element method (FEM) is a numerical technique for finding approximate solutions of partial differential equations (PDE) as well as of integral equations [12].

The solution approach is based either on eliminating the differential equation completely (steady state problems), or rendering the PDE into an approximating system of ordinary differential equations, which are then numerically integrated using standard techniques such as Euler's method, Runge-Kutta etc. Using the simplest finite element given by linear quadrilateral (for two-dimensional image data) or by linear parallelepiped (for three-dimensional image data) with nodal points coincident with the centres of the image elements an approximate solution ϕ^h of ϕ will be easily obtained for any image data $v \in \mathcal{V}$ and segmented image $u \in U$. Using this solution, a finite element approximation of the topological derivative takes the form,

$$D_{T^h}(\hat{x}) = \tfrac{1}{2}(c_i - u^h)\left[\left(\varphi^h(\hat{x}) - (v^h - u^h)\right) + \left(\varphi^h(\hat{x}) - (v^h - c_i)\right) + 2(1-\beta)\varphi^h(\hat{x})\right] \forall \hat{x} \in \Omega \quad (16)$$

Where v^h and u^h are the finite element interpolation at point $\hat{x}$ of the functions v and u respectively. Furthermore, considering that the topological derivative depends on c_i let us denote by $\widehat{ci}$ the class c_i which minimizes $D_T{}^h(\hat{x})$ that we will also denote by $\widehat{D_{T^h}(\hat{x})}$. As mentioned before, according to the topological asymptotic expansion in (1), for an image data $v \in \mathcal{V}$ we must find the segmented image $u^* \in U$ which minimizes the cost functional $\mathcal{J}$ by successively choosing the class that produces the most negative values of the topological derivative [12].

2.3 Contouring Scheme

The contour approaches [13] are widely used in practical exploitation of data from images because they effectively use specific prior information about objects and this makes them inherently efficient algorithms. Furthermore, active contours apply processing algorithms selectively to regions of the image, rather than processing the entire image [8]. In general, the energy function of contour model (snake) [14] can be given by

$$E = \int_0^1 \left[\frac{1}{2}[\alpha|x(s)|^2 + \beta|x(s)|^2] + E_{ext}(x(s))ds\right] \quad (17)$$

Where, α is the tension, β is the rigidity factor, E_{ext} is the external energy and x(s) are the snake points. The energy of the image is positive in homogeneous regions and non-zero at the sharp edges. The edge function can be modeled as

$$g(|\bar{v}u|) = \frac{1}{1 + |G_\sigma * U|^p} \quad (18)$$

Where g is a positive decreasing function, U is the image to be segmented, G_σ is the 2-D Gaussian kernal and 'P' is an integer (normally chosen to be 2). These equations can be solved to obtain the new snake coordinate points X and Y.

$$\mathbf{x}^{\langle i+1\rangle} = \left(\mathbf{A} + \frac{1}{\Delta}\mathrm{I}\right)^{-1}\left(\frac{1}{\Delta}\mathbf{x}^{\langle i\rangle} + fx(\mathbf{x}^{\langle i\rangle}, \mathbf{y}^{\langle i\rangle})\right) \quad (19)$$

$$\mathbf{yx}^{\langle i+1\rangle} = \left(\mathbf{A} + \frac{1}{\Delta}\mathrm{I}\right)^{-1}\left(\frac{1}{\Delta}\mathbf{yx}^{\langle i\rangle} + fy(\mathbf{x}^{\langle i\rangle}, \mathbf{y}^{\langle i\rangle})\right) \quad (20)$$

where A is the first order differential of the edge magnitude along X-axis and Y-axis respectively. These equations can be solved to arrive at the new vector which controls the moment of the snake.

3 Results and Discussion

The performance of shape sensitive derivative approach and region growing are compared here. The characterization of the lesion into benign and malignant is done based on the characteristics of the contour and features of the segmented lesion.

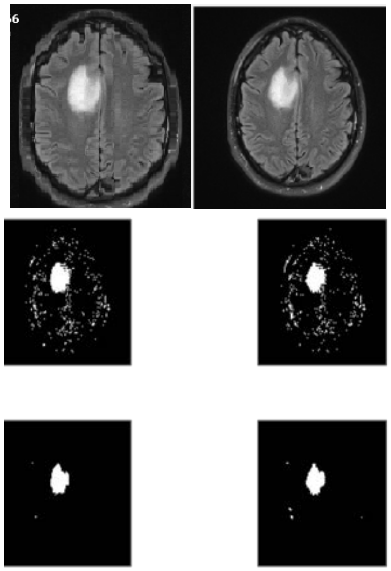

Figure 1: Original and Segmented glioma images

Ten MR image data sets, comprising four true positive glioblastoma multiforme and six true negative, which are benign lesions, of T1 contrast T2weighted and FLAIR sequences has been analysed for Statistical parameters, sensitivity, specificity, positive predictive value and negative predictive value, to evaluate the efficacy of the proposed segmentation method. The geometric features like irregularity of the boundary carries information regarding tumor growth rate prognosis. Such shape based features acting as input to the classifier determine the accuracy of the classification. The accuracy of these shape based features depends on the efficiency of segmentation to preserve the characteristics boundary of ROI. The statistical evaluation indices used to evaluate the features are estimated as sensitivity = number of TP/number of cancer cases; specificity= number of TN/number of non-cancer cases; positive predictive value (PPV) = number of cancer cases/ (number of TP+FP cases); and negative predictive value (NPV) = number of non-cancer cases/ (number of FN+TN). It is expected that the classification efficiency is the mere reflection of the statistical significance of the feature used for classification. It is perspective that the hybrid approach is exhibiting the highest performance index.

Table 1: Statistical Performance Indices

	LDA	DA+SVM
Sensitivity	69%	90%
Specificity	77.08%	93.3%
Positive Predictive Value	1.35	1.61
Negative Predictive Value	0.52	0.94
Region Growing Technique		
Sensitivity	62%	83%
Specificity	76%	91.3%
Positive Predictive Value	1.15	1.52
Negative Predictive Value	0.45	0.92

The numerical values of the sensitivity, specificity, positive and negative predictive values of LDA and DA+SVM classifiers for both of the segmentation schemes are shown in table 1. The original axial plane MR images lesions and the segmented lesions before and after morphological operations are shown in figure 1. From the graphical illustration in figure 2, it is obvious that the classification DA + SVM overrides LDA

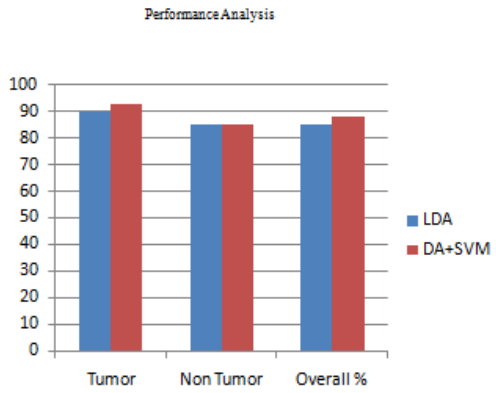

Figure 2: Classification efficiency

4 Conclusion

The lesions in the MR images were characterized into benign and malignant ones using shape based features extracted from the segmented lesions. The performance of region growing and sensitive derivative approaches were compared in preserving the geometrical features of the contour. The feature extracted from the segmented lesions were used as input to LDA and DA+SVM classifiers. Shape sensitive derivative approach will preserves the characteristics of the lesion boundary than region growing. The sensitivity, specificity, positive and negative predictive values of shape sensitive derivative segmentation method is more than the region growing. The DA+SVM has better classification ability than LDA.

ACKNOWLEDGEMENT

The authors would like to thank Dr. Jose Tom (Professor & Head, Department of Radiotherapy, Government Medical College, Kottayam, India), Dr. Unni. S. Pillai (Department of Oncology, The Jawaharlal Institute of Postgraduate Medical Education & Research (JIPMER), India), Dr. Gowri Shanker (Hindlab, Govt. Medical College, Kottayam, India) for their incessant involvement in this endeavor.

REFERENCES

[1]. W. Gonzalez, Digital Image Processing, 2nd ed. Prentice Hall, Year of Publication, 2008: 378.

[2]. M.LToure, Advanced Algorithm for Brain Segmentation using Fuzzy to Localize Cancer and Epilepsy Region, International Conference on Electronics and Information Engineering (ICEIE) 2010.2.

[3]. OZ.Shi and K.B.Fung, A Comparision of Digital Speckle Filter in proc. IEEE on IGARSS, 1994.4: 2129 – 2133.

[4]. MMancas, BGosselin, Benoîtmacq, Segmentation Using a Region Growing Thresholding Proc. SPIE 5672, Image Processing: Algorithms and Systems IV, 2005:388.

[5]. SanthiyaKumari.N and M.Madheswaran, Analysis of Arthrosclerosis for identification of cerebro-vascular and cardiovascular diseases using active contour segmentation of carotid artery, Proceedings of International symposium on global trends in Bio-medical Informatics, Research, Education and Commercialization, SBRI, India, 2008.

[6]. Djerou, L., Khelil, N., Batouche, M., Image Segmentation by Self-Organised Region Growing, Computer Information Systems and Industrial Management Applications, CISIM '08. 2008:171-176.

[7]. WankaiDeng , Wei Xiao, Chao Pan, J Liu Key , MRI brain tumor segmentation based on improved fuzzy c-means, Method. Laboratory of Education Ministry for Image Processing and Intelligence Control Institute for Pattern Recognition and Artificial Intelligence SPIE, 2009.7497.

[8]. Auroux, M. Masmoudi, and L. Belaid, Image restoration and classification by topological asymptotic expansion, Variational Formulations in Mechanics: Theory and Applications - CIMNE, Barcelona, Spain 2006.

[9]. Larrabide.I, A. A. Novotny, R. A. Feijo, and E. Taroco, A medical image enhancement algorithm based on topological derivative and anisotropic diffusion,in Proceedings of the XXVI Iberian Latin-American Congress on Computational Methods in Engineering - CILAMCE ,2005.

[10]. Novotny.A, R. Feij´oo, E. Taroco, and C. Padra, Topological sensitivity analysis, Computer Methods in Applied Mechanics and Engineering, 2003. 192: 803–829.

[11]. Kelly H Zou, Statistical Validation of Image Segmentation Quality Based on a Spatial Overlap Index, AcadRadiol. 2004. 11(2): 178–189.

[12]. Ignacio Larrabide, Antonio, Masmoudi, et.al, Topological Derivative as a tool for image processing, Part I, National Laboratory for Scientific Computation, Petr´opolis, Brazil, 2006.

[13]. J Xu, A Janowczyk, S Chandran, A Madabhushi, A high-throughput active contour scheme for segmentation of histopathological imagery, Medical Image Analysis, 2011.15(6): 851-862

[14]. G Xu, E Segawa, S Tsuji, Robust active contours with insensitive parameters, Pattern Recognition, 1994.27(7):879-884

SOCIETY FOR SCIENCE AND EDUCATION UNITED KINGDOM

JBEMi JOURNAL OF BIOMEDICAL ENGINEERING AND MEDICAL IMAGING

ISSN: 2055-1266
VOLUME 1, ISSUE 6

Computer-aided Diagnosis for Internal Hemorrhoids by Measuring the Congestive Extent in Endoscopic Images

Koji Abe[1], Hidenori Takagi[2], Masahide Minami[3] and Haiyan Tian[4]

[1]*Department of Informatics, School of Science and Engineering, Kinki University, Japan*;
[2]*Interdisciplinary Graduate School of Science and Engineering, Kinki University, Japan*;
[3]*Graduate School of Medicine, The University of Tokyo, Japan*;
[4]*Graduate School of Engineering, Kobe University, Japan*;
[1]koji@info.kindai.ac.jp, [2]tkghdnr2@gmail.co.jp, [3]maminami@dream.com, [4]tian.haiyan2006@gmail.com

ABSTRACT

This paper presents a system of computer-aided diagnosis for internal hemorrhoids based on the congestive extent using endoscopic images. This system could be effective for young or even general practitioners as a second opinion. In the proposed method, a pre-processing is conducted to the images for enhancing saturation and contrast of congestive regions and blood vessels. Next, considering characteristics of internal hemorrhoids, the proposed method measures degree of the congestion in the images, and extracts the congestive region and abnormalities on the congestive extent. Experimental results of the discrimination using the proposed abnormalities between normal and abnormal cases for 204 images including 108 abnormal cases have shown that the abnormalities are well effective to diagnose the congestion in the hemorrhoids.

Keywords: Computer-aided diagnosis; Internal hemorrhoids; Congestion; Medical image processing; Endoscopic image.

1 Introduction

Internal hemorrhoids are one of diseases in the anus. The hemorrhoids come from the congestion of the blood caused by sitting for long time at work, baby care, etc. With labor circumstances in the times, at least 70-80 % of population in developed countries could potentially have symptoms of the hemorrhoids. However, since there is no nerve in the rectum, most of people hardly notice the symptoms and the hemorrhoids have been already progressing when we feel the symptoms. The early stage of the hemorrhoids is the congestion, and the symptom changes into appearance of projection and swellings, and then folds with the progression of the hemorrhoid. Therefore, the congestion is the most fundamental symptom in hemorrhoids.

When diagnosticians check internal hemorrhoids, they insert the endoscope from the anus into the rectum. Scenes of the rectum taken by the endoscope are shown to them via a monitor. At that time, if diagnosticians confirm a lesion of internal hemorrhoids, they save several endoscopic images of the lesion as a material for future observations. However, since it is difficult for even experts on hemorrhoids to diagnose internal hemorrhoids, disagreement between diagnosticians is often

DOI: 10.14738/jbemi.16.676
Publication Date: 05th December 2014
URL: http://dx.doi.org/10.14738/jbemi.16.676

happened. For the reasons, a computer-aided diagnosis (CAD) system for evaluating internal hemorrhoids is required as a second opinion for diagnosticians. Measuring abnormality of the congestion in internal hemorrhoids could be useful for an assisted system for new doctors and non-experts.

Diagnosticians judge the congestion in internal hemorrhoids based on only their experience after they observe the color and the size of the congestive part. Although there is no report on extracting abnormalities for the congestive region in medical images, as similar trials in the field of medical image processing, recognition of lesions [1, 2], segmentations of organs or objects such as bleeding regions [3–6], etc. have been reported. However, all of them are effective to only cases when contours of recognition parts are clear in images. Since the contour of the congestion is not clear in many cases due to shade around the contour, it would be difficult to apply them to the extraction of the congestion area. And, even if another technique to recognize an object in a gradation area like landscape images were existed, it would be hard to recognize the congestive region in endoscopic images because boundary between the region and its background is very dark in most cases due to shade, i.e., characteristics of color are hardly appeared around the boundary.

To design a CAD for internal hemorrhoids, this paper proposes a method for extracting the congestive extent of the hemorrhoids as abnormalities from endoscopic images. In addition, using the abnormalities, the proposed method diagnoses the images by discriminating between normal and abnormal cases as a prototype of the CAD. The abnormalities are measured by extracting characteristics of density distribution in the images. And then, this paper examines performance of the abnormalities from experimental results obtained by the discriminations.

2 Endoscopic Images of Internal Hemorrhoids and the Congestion of the Blood

Symptoms of internal hemorrhoids appeared in the endoscopic image are broadly divided into the following three: 1) the congestive region appears around the tube or its tip, 2) projections or swellings appear around the tube with the anal canal opened, and 3) the folds appear around the tube due to hard projections and swellings. Figure 1 shows an example of each case, where the leftmost is a normal case and the other three are abnormal cases. And, the black cylindrical object in every image shown in Figure 1 is the tube of the endoscope. In the normal case, the whole color of internal rectum looks pink and there is no significant difference of color between the whole color and the area around the tube. On the other hand, as shown in the image of “congestion” in Figure 1, we can see the color is changed into blackish purple around the tube. This part is the congestive region of the blood and a main factor to diagnose internal hemorrhoids caused by the congestion. Basically, the congestive region is taken around the tube in endoscopic images. When a diagnostician take a picture in the rectum using an endoscope, sometimes the tube is not appeared in the image depending on location of the taking place and camera lens. Considering the characteristic of the congestion in the image, only the images which include the tube region are used in this research.

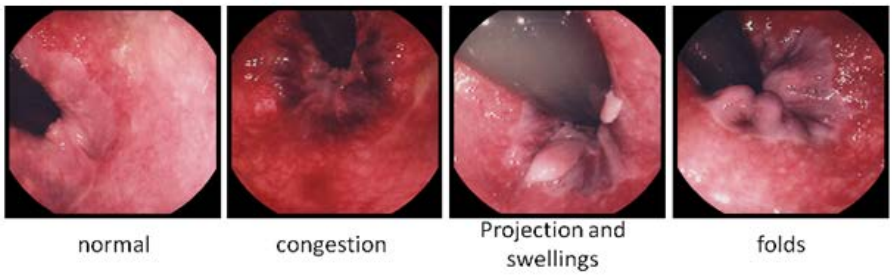

Figure 1: Typical cases of internal hemorrhoids

To the endoscopic images, this paper proposes features for measuring the congestion extent such cases shown at "congestion" in Figure 1. Figure 2 shows difference of the histogram on each of red and blue values in RGB color space between a normal part and a congestive part, where the size of both of the two rectangles in the image is 40×60; and the histograms have been measured in each of the areas. In addition, Table 1 shows the mean values and the standard deviations for the histograms. From Figure 2 and Table 1, we can confirm that difference between red and blue values in the congestive part is much smaller than normal part, and red values in the congestive part are lower than normal part.

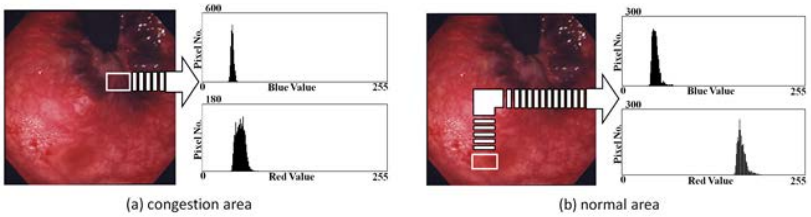

Figure 2: Difference of color between the congestive region and normal area.

Table 3: The Mean value and the standard deviation of the histograms show in Fig. 2.

	Mean value	Standard deviation
red value in (a)	55.4	32.7
red value in (b)	174.6	36.4
blue value in (a)	44.0	57.3
blue value in (b)	48.8	41.2

3 Proposed Method

Throughout this paper, the size of all the images is 512×512 pixels with 24-bit full color.

3.1 Preprocessing

First, since the color of the tube region in the image is nonrelative in recognition of the congestive region and feature extractions of the congestive extent, and besides, there is possibility the region could be a noise due to much halation, the tube region is extracted from the original image by the Lazy Snapping (LS) [7] and all the pixel values in the tube region are converted into black color (i.e., the tube region is removed from the original image). The extraction is conducted according to the manual shown below. LS is a method for separating an image into the target area and its background by roughly drawing the boundary between them with an interface, hence the user manually cuts the target drawing

a boundary between the two areas with a mouse or a tablet-pan on the monitor. Figure 3 shows a case when LS is applied to one of the endoscopic images, where (1) is the original image, (2) is a curve drawn in the inside of the tube region along the tube contour, (3) is a curve drawn in the outside of the tube region along the contour, and (4) is the final output. As shown in Figure 3(4), only the color of tube region is converted into black color. The manual and Figure 3 are shown to the user as a guide for drawing the curves.

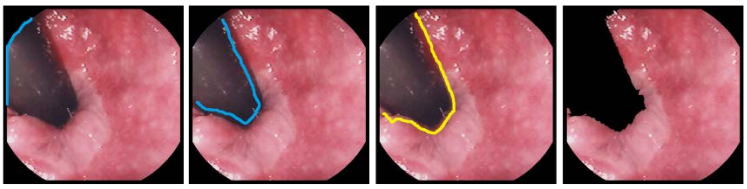

Figure 3: Extraction of the tube region by the Lazy Snapping.

[*Manual for extracting the tube region*]

1. Draw a blue curve on the tangential line of the tube region and the frame of the image.

2*. Draw a blue curve inside of the tube region along the counter of the tube region.

3*. Draw a yellow curve outside of the tube region along the counter of the tube region.

*Be careful not to draw the curves on the tube edge or the outside flame of the image.

Next, to the image conducted the tube removal, pixel values in RGB space are converted into HSV space and the linear stretch with saturation is conducted. In the stretch, the histogram for saturation value *S* is stretched at the range [0, 1]. After the stretch, pixel values are reconverted into values in RGB space. Figure 4 shows a case when the stretch is conducted, where the left is an image before the stretch and the right is the converted image. By this conversion, the congestion area and blood vessels could be brighter. RGB values are converted into HSV values *H* (hue), *S* (saturation), and *V* (value) as follows:

$$H = 60 \times \begin{cases} \dfrac{G-B}{max-min} & if\ \ max\ is\ R \\ \dfrac{B-R}{max-min} + 120 & if\ \ max\ is\ G \\ \dfrac{R-G}{max-min} + 240 & if\ \ max\ is\ B \end{cases} \tag{1}$$

$$S = \frac{max-min}{max} \tag{2}$$

$$V = max \tag{3}$$

where *R*, *G*, and *B* are color values of red, green, and blue in the pixel, respectively; and *max* and *min* are the highest and the lowest values among *R*, *G*, and *B*.

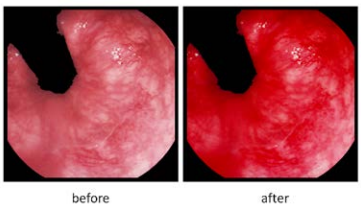

Figure 4: The linear stretch with saturation.

3.2 Extraction of an abnormality on Congestion: f_1

As shown in Figure 2, red values of the blackish purple color appeared in the congestive region are basically higher than blue values. However, supposing features of the congestive extent were extracted considering only this characteristic, there could be possibility that halation and light-colored area become strong noises in the extraction. Besides, the red values are generally lower than red values in normal area. Considering them, an abnormality on congestion f_1 is given by

$$f_1 = \sum_{x=0}^{512} \sum_{y=0}^{512} P(x,y) \tag{4}$$

$$P(x,y) = \frac{B(x,y)}{R(x,y)} \times w_R(x,y) \tag{5}$$

Where $w_R(x, y)$ ($0 \le w_R(x, y) \le 1$) is the weight determined by red value R and blue value B in the pixel (x, y). Thus, f_1 would be an abnormality considering the size of the congestive region and its color because f_1 measures the shade of the blackish purple with the ratio of B for R to all the pixels in the image.

3.2.1 Derivation of the *Weight* $w_R(x, y)$

The weight w_R in the pixel (x, y) is determined by employing the following sigmoid function:

$$w_R(x,y) = \frac{1}{1+e^{-a(-127+R(x,y)-axis)}} \tag{6}$$

Where a is the gain value of the function, $R(x, y)$ is red value in the pixel (x, y), and *axis* is defined as x-coordinate at the axis of symmetry in the sigmoid curve. The reason why the sigmoid function is employed is because the abnormality would be more effective in the discrimination between normal and abnormal cases if we could arrange difference of abnormality between normal and abnormal cases as much as possible around the boundary between groups of normal case and abnormal case. Therefore, the more $R(x, y)$ is small, the more w_R is large (i.e., w_R approaches 1), hence f_1 is going to the ratio of B for R shown in Eq.(5). On the other hand, the more $R(x, y)$ is large, the more w_R is small (i.e., w_R approaches 0), hence the ratio is revised low and f_1 is held down. As an example of the sigmoid function given by Eq.(6), Figure 5 shows a sigmoid curve for Eq.(6) where a and *axis* are 0.5 and 0, respectively.

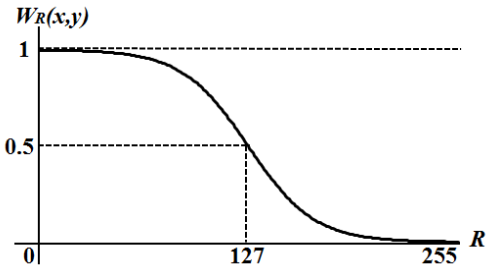

Figure 5: Sigmoid curve for Eq.(6) (a: 0.5, *axis*: 0)

3.2.2 Determination of the parameters *a* and *axis* in the weight $w_R(x, y)$

The parameters a and axis are determined using samples. The samples should be chosen evenly from each dataset of normal and abnormal cases. In order to choose the samples evenly in the vector space, principal component analysis is applied to all the images in each case separately. The variables for the analysis are regarded as the three color values in RGB. By the analysis, the images are represented as vectors which have three coordinates of the first, second, and third principal components in a 3D space composed of the components. Putting all the images in each class in the 3D space, the image which is the nearest vector from the mean vector in each of the 8 quadrants in the 3D space is selected, i.e., 8 images are selected as the samples from each dataset of normal and abnormal cases (i.e., 16 images are totally selected.). Second, using f_1 extracted from the samples, degree of separation between the couple of datasets composed of the samples in each case is calculated. The degree of separation *Sep* is given by

$$Sep = \frac{\partial_b^2}{\partial_w^2} \tag{7}$$

$$\partial_b^2 = \frac{N_n N_a (m_n - m_a)^2}{(N_n + N_a)^2} \tag{8}$$

$$\partial_w^2 = \frac{N_n \partial_n^2 + N_a \partial_a^2}{N_n + N_a} \tag{9}$$

Where N_n and N_a are the number of the samples in each of normal and abnormal cases ($N_n = N_a = 8$), m_n and m_a are the mean value of f_1 extracted from the samples in each, ∂^2_n and ∂^2_a are variance of f_1 in each, respectively. Third, changing both values of *axis* in the range [-127, 127] (pitch: 1) and *a* in the range [0.1, 10.0] (pitch: 0.1), *Sep* is calculated each time. And then, the couple of *a* and *axis* used in the case when *Sep* obtains the largest value is determined as their optimum values at last.

3.3 Extraction of the Congestive Region

The congestive region is extracted by the linear discriminant analysis with $P(x, y)$ shown in Eq.(5). The discriminant analysis is applied to every pixel in the image and their discriminant score decides whether the pixel belongs in the congestive region or its background. If the score for a pixel is more than 0, the pixel belongs in the congestive region. Figure 6 shows the extracted congestive region for a case, where (1) is the original image, (2) is the extracted congestive region.

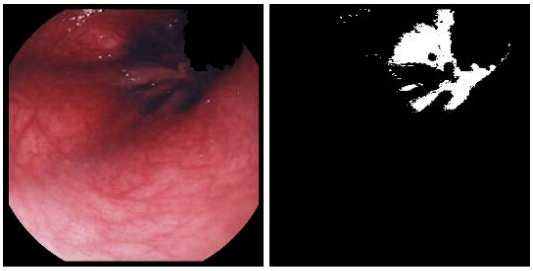

(1) (2)

Figure 6: Extraction of the congestive region for a case.

3.4 Extraction of the abnormalities: f2, f3, and f4

In addition to f_1 proposed in **3.2**, the other abnormalities on the congestive extent f_2, f_3 and f_4 are extracted as features from the extracted congestive region obtained in **3.3**. f_2 represents the size of the congestive region. f_3 represents the mean value of red values in the congestive region. And, f_4 represents the mean value of the ratio of the blue values for the red values in the congestive region. Now, when the number of pixels in the congestive region is *size* and one of them is represented by c_i ($1 \le i \le size$), the abnormalities are given by

$$f_2 = size \tag{10}$$

$$f_3 = \frac{1}{size}\sum_{i=1}^{size} r_i \tag{11}$$

$$f_4 = \frac{1}{size}\sum_{i=1}^{size} \frac{b_i}{r_i} \tag{12}$$

where r_i and b_i are the red and the blue values of the pixel c_i, respectively.

4 Experimental Results

To examine performance of the proposed abnormalities, linear discriminant analysis (LDA), neural network (NN), linear support vector machine (L-SVM), and nonlinear support vector machine (N-SVM) were applied to the discrimination of the endoscopic images into normal or abnormal (i.e., internal hemorrhoids) cases by regarding the abnormalities as variables, respectively. Each of the abnormalities was normalized to the dataset that the mean value is 0 and the variance is 1. NN was designed as a three-layered perceptron (input layer: 3, hidden layer: 5, output layer: 3), where sigmoid function and back propagation (learning rate: 0.3, weight decay rate: 0.1) were used. As a kernel function in N-SVM, the Gaussian kernel was used.

Selecting the samples for each of normal and abnormal cases from the dataset, the parameters *a* and *axis* in Eq.(6) were obtained. Figure 7 shows *Sep* vs. the parameters *a* and *axis*. From the result shown in Figure 7, the parameters *a* and *axis* were obtained as 4.1 and -2, respectively. The number of the images is 204 (normal case: 96, abnormal cases: 108), where the 16 samples selected to determine *a* and *axis* were removed. In the experiments, each of three users A, B, and C, which are non-expert, drew the curves for the tube region seeing Figure 3 and the manual shown in 3.1, and the experiments were conducted to each of the users.

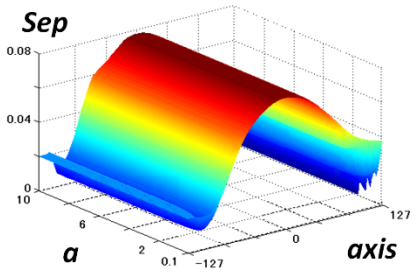

Figure 7: *Sep* vs. *a* and *axis*.

The training dataset and test dataset were chosen by the leave-one-out cross validation [8] in all the discriminations. In fact, every discrimination was conducted as the following procedure:

1. Choose 1 image from all the images as test data, and use the other images as training dataset.
2. Discriminate the test data between the class of “normal” and “abnormal”.
3. Changing the test data, repeat from 1 to 2 until every image has been the test data.

Table 2 shows discrimination results for abnormal and normal cases respectively obtained by the three discrimination machines of LDA, NN, and L-SVM, where *Precision* and *Recall* represent the discrimination ratio. They are defined as

$$Precision = \frac{X_{h \cap c}}{X_c} \times 100 \tag{13}$$

$$Recall = \frac{X_{h \cap c}}{X_h} \times 100 \tag{14}$$

Where X represents the number of images, X_h is the number of the correct answers, and X_c is the number of images discriminated by the proposed method. In addition, Figure 8 shows the discrimination ratios against change of the parameter ð in the Gaussian kernel used in N-SVM, where A and N means abnormal and normal cases, respectively. As shown in Table 2 and Figure 8, the discrimination ratios for each of normal and abnormal cases show more than 80 % and there is no significant difference of the results between the users. Actually, in order to pass the reading test of mammography images in Japan, medical doctors have to correctly read at least 80 % in each of cancer cases and normal cases. Hence, if the experimental results were evaluated from the clinical standpoint, the experimental results would show the proposed abnormalities are appropriately extracted for the discrimination of internal hemorrhoids caused by the congestion. Table 3 shows the mean value of each abnormality extracted from correct dataset of each case, where the number in the round blankets is the standard deviation.

Table 2: Experimental results

User	case	LDA		NN		SVM	
		Precision	*Recall*	*Precision*	*Recall*	*Precision*	*Recall*
A	normal	85.4%	78.1%	83.3%	82.5%	80.5%	80.6%
	abnormal	78.7%	85.9%	84.3%	85.0%	81.5%	87.1%
B	normal	89.6%	81.1%	85.4%	85.4%	87.5%	82.4%
	abnormal	81.5%	89.8%	87.0%	87.0%	83.4%	88.2%
C	normal	84.4%	72.3%	86.5%	83.8%	87.5%	80.0%
	abnormal	71.3%	83.7%	85.2%	87.6%	80.6%	87.9%

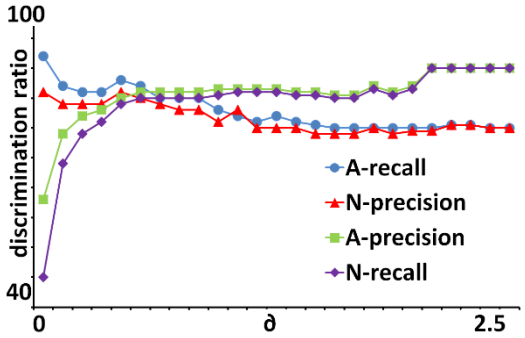

Figure 8: The discrimination ratio vs. ∂ of the Gaussian kernel in N-SVM

Table 3: Mean values of the abnormalities in each of correct abnormal and normal datasets. (The number in the parenthesis is the standard deviation.)

abnormality	f_1	f_2	f_3	f_4
abnormal	0.55 (1.10)	0.57 (1.03)	-0.55 (0.80)	0.59 (0.99)
normal	-0.61 (0.17)	-0.64 (0.39)	0.62 (0.81)	-0.66 (0.42)

Figure 9 shows an example of discrimination success for the abnormal case in all the discrimination machines. In Figure 9, (1) is the original image, (2) is the image where the tube has been removed from (1), (3) is the image converted by the stretch with saturation for (2), and (4) is the black and white image of congestive region extracted from (3), where the region is shown as the white color. In addition, Figure 10 shows an example of discrimination success for the normal case in all the discrimination machines, where (1), (2), (3) and (4) are the same as Figure 9, respectively.

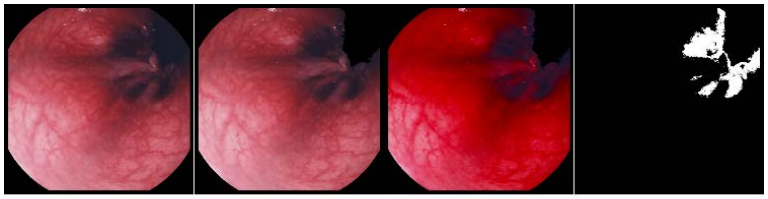

Figure 9: An abnormal case of discrimination success (f1 = 0.100, f2 = 0.199, f3 = -0.741, f4 = 0.174).

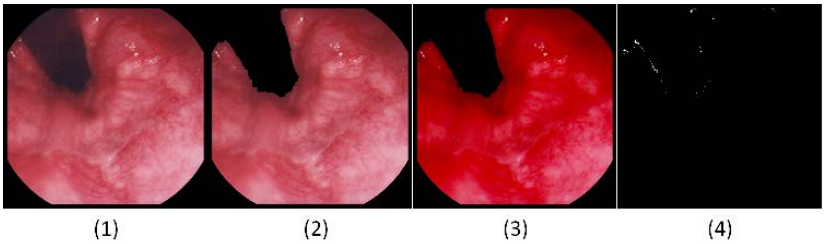

Figure 10: A normal case of discrimination success (f_1 = -0.766, f_2 = -1.003, f_3 = 1.574, f_4 = -1.273).

5 Discussions

In the experimental results, the number of images which were discrimination failure in all the discrimination machines was 15, where 7 normal cases were diagnosed as abnormal cases and 8 abnormal cases were done as normal cases. Figure 11 – 14 show examples of the discrimination failures, where (1), (2), (3) and (4) are the same as Figure 9, respectively.

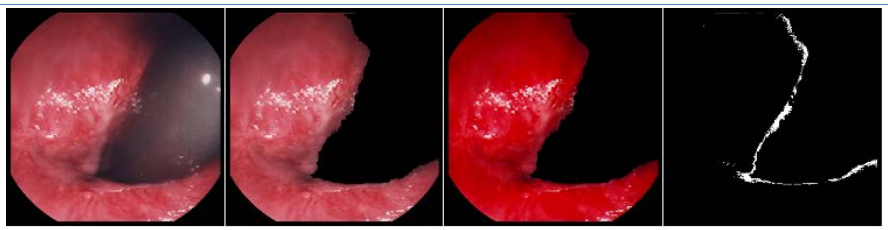

Figure 11: Failure case 1 (by the proposal: abnormal, correct answer: normal)

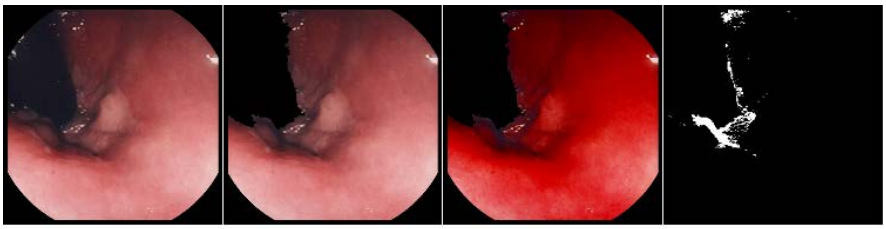

Figure 12: Failure case 2 (by the proposal: abnormal, correct answer: normal)

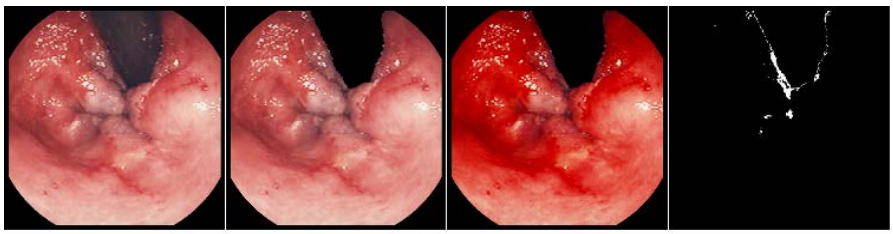

Figure 13: Failure case 3 (by the proposal: normal, correct answer: abnormal)

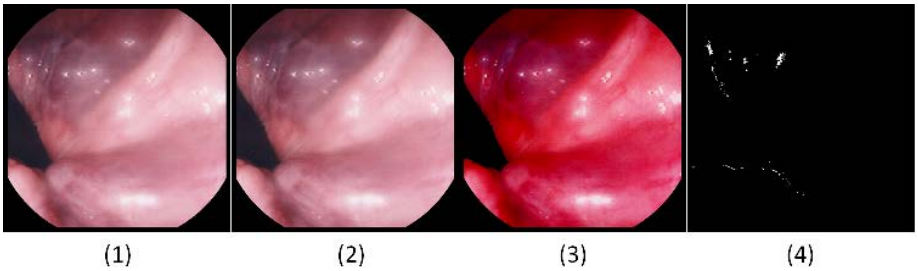

Figure 14: Failure case 4 (by the proposal: normal, correct answer: abnormal)

The normal cases which were diagnosed as abnormal cases can be divided broadly into two kinds. Figure 11 and Figure 12 show a case of each kind. In the case of Figure 11, we could confirm there is the congestive region though this case is a normal case, besides f1=-0.226 and f2=0.446, i.e., the features are closer to the mean value of them in abnormal case shown in Table 3. Actually, this case was internal hemorrhoids before and it is going to the recovery in progress; and a diagnostician concluded this case has already gone out of abnormal cases. The other 3 normal cases were the same as this. In the case of Figure 12, we can confirm that there is shade such as shadow appeared like a tunnel. Since the proposed method cannot distinguish between the congestive region and the shade, the proposed method cannot extract the features precisely in this kind of cases when deep shade is appeared around the tube. In fact, f3 and f4 are -0.301 and 0.067, respectively, and they are closer to the mean values of them in abnormal

case than normal case shown in Table 3. The other 2 normal cases were the same as this. In the future, it is necessary to consider a method for recognizing bumpy surface and its color in the endoscopic images.

Next, the abnormal cases which were diagnosed as normal cases can be also divided broadly into two kinds. Figure 13 and Figure 14 show a case of each kind. In the case of Figure 13, we can confirm there are some projections and swellings. Since the proposed abnormalities are designed by considering only the congestion, the abnormalities cannot apply to these symptoms. Regarding the image shown in Figure 13, the abnormalities are f_1=-0.633, f_2=-0.669, f_3=0.412, and f_4=-0.486, respectively, and all of them are closer to the mean values of normal cases shown in Table 3. The other 3 abnormal cases were the same as this. In the future, it is necessary to consider a method for recognizing the projection and swelling parts in order to diagnose these symptoms separately. In the case of Figure 14, due to the lightning of the endoscope, change of hue has been occurred hence the abnormal case was discriminated as a normal case. The other 3 abnormal cases were the same as this. Regarding the image shown in Figure 14, the abnormalities are f_1=-0.755, f_2=-1.018, f_3=0.885, and f_4=-0.208, respectively, and all of them are closer to the mean values of normal cases shown in Table 3. The lightning sometimes brings halation or change of hue into endoscopic images. If the location of the light source could be obtained, there could be possibility that the color of the image is reproduced into the original color. However, since this problem can also occur in other general images and it is still not solved, in order to cope with this case, it might be necessary to consider preparing a manual on taking desirable pictures for diagnosticians.

6 Conclusions

Aiming at showing a second opinion to diagnosticians and supporting non-experts in internal hemorrhoids, this paper has presented abnormalities for measuring the congestive extent in endoscopic images of internal hemorrhoids. The proposed abnormalities provide degree of congestive color density and size of the congestive region as features besides they could be used for a computer-aided diagnosis of internal hemorrhoids. Regarding the abnormalities as variables for discrimination of internal hemorrhoids, this paper has examined performance of the abnormalities by discriminating between normal and abnormal cases with discrimination machines. Experimental results of the discriminant trials have shown that the discrimination ratios for the proposed method have become more than 80 % in almost of the trials. In addition, we have confirmed the proposed method could extract the congestive region well. However, the proposed method cannot still cope with abnormal cases caused by the other symptoms. And also, it is difficult to diagnose internal hemorrhoids to the images where hue have been changed due to the light of the endoscope.

Therefore, as future works, it is necessary to consider recognizing bumpy surface and its color in the images, the projection and swelling parts, and designing a manual on taking the desirable pictures for diagnosticians.

REFERENCES

[1]. B. Li and M.Q. Meng (2009), 'Computer-Aided Detection of Bleeding Regions for Capsule Endoscopy Images', *IEEE Trans. Biomed. Eng*., **56**(4), 1032-1039.

[2]. K-B Kim, S. Kim, and G-H Kim (2006), 'Analysis System of Endoscopic Image of Early Gastric Cancer', *IEICE Trans. Fundam. Electron. Commun. Comput Sci*., **E89-A**(10), 2662-2669.

[3]. M.P. Tjoa, S.M. Krishinan, C Kugean, P. Wang, and R. Doraiswami (2001), 'Segmentation of Clinical Endoscopic Image Based on Homogeneity and Hue', *Proc. Annual Int. Conf. IEEE Eng. Med. Biol. Soc*., **3**, 2665-2668.

[4]. M. Xiao, S. Xia, and S.Wang (2005), 'Geometric Active Contour Model with Color and Intensity Priors for Medical Image Segmentation', *Proc. 27th Annual Int. Conf. IEEE Eng. Meg. Biol. Soc*., 6496-6499.

[5]. H. Tian, T. Srikanthan, and K. V. Asari (2001), 'Automatic segmentation slgorithm for the lumen region and boundary from endoscopic images', *Med. Biol. Eng. Comput*., **39**(1), 8-14.

[6]. F. Vilarino, P. Spyridonos, F. Deiorio, J. Vitria, F. Azpiroz, and P. Radeva (2010), 'Intestinal Motility Assessment With Video Capsule Endoscopy : Autmatic of Phasic INtestial Contractions', *IEEE Trans Med Imaging*, **29**(2), 246-259.

[7]. Y. Li, J. Sun, C-K Tang, and H-Y Shum (2004), 'Lazy Snapping' , *ACM Trans. on Graphics*, **23**(3), 303-308.

[8]. M. Stone (1974), 'Cross-Validatory Choice and Assessment of Statistical Predictions', *J. of the Royal Statistical Society*, *Series B (Methodological)*, **36**(2), 111-147.

SOCIETY FOR SCIENCE AND EDUCATION UNITED KINGDOM

JBEMi JOURNAL OF BIOMEDICAL ENGINEERING AND MEDICAL IMAGING

ISSN: 2055-1266
VOLUME 1, ISSUE 6

Features for Discriminating Normal Cases in Mass Screening for Gastric Cancer with Double Contrast X-ray Images of Stomach

[1]Koji Abe, [2]Hideaki Nakagawa, [3]Masahide Minami and [4]Haiyan Tian

[1]Department of Informatics, School of Science and Engineering, Kinki University, Japan;
[2]Interdisciplinary Graduate School of Science and Engineering, Kinki University, Japan;
[3]Kanazawa Gakuin University, Japan;
[4]Graduate School of Engineering, Kobe University, Japan;
[1]koji@info.kindai.ac.jp, [2]nakagawa0623nara@gmail.com, [3]maminami@dream.com,
[4]tian.haiyan2006@gmail.com

ABSTRACT

In a mass screening for gastric cancer, diagnosticians read many stomach X-ray pictures at a time. To decrease the number of reading the pictures in the mass screening, the proposed method discriminates normal cases in stomach X-ray images using the proposed features. In the normal cases, folds on the stomach wall appear in parallel in the images. Considering this characteristic, the proposed method measures parallelism of the folds in the images. Experimental results of the discriminations for 88 images where 13 abnormal cases are included have shown that the proposed features are well effective for recognizing normal cases.

Keywords: Computer-aided diagnosis; Gastric cancer; Double contrast X-ray image of stomach; Medical image processing.

1 Introduction

In mass screenings for gastric cancer, due to financial reasons, double contrast X-ray pictures are generally used on behalf of CT, MRI or photogastroscope. In the screenings, diagnosticians always need a hard labor because they read several hundred X-ray pictures at a time. Besides, since accuracy of the reading is strongly depended on experience of diagnosticians, it is hard for inexperienced doctors to read them well. For the reasons, CAD (computer-aided diagnosis) systems for gastric cancer in X-ray images have been required as a second opinion for diagnosticians [1-5]. The existing systems mark the location of lesions in X-ray images which show an abnormal case [2-5]. In gastric X-ray images, since a cancer part appears as a pattern that lines concentrate at a spot in a stomach area, the existing systems detect the part by measuring degree folds concentrate or applying a filter for emphasizing the concentration part in the images. However, the systems cannot reduce the hard labor due to lack of accuracy in the marking. Besides, to diagnose characteristics of legions, since diagnosticians have to directly read pictures of abnormal cases even though the systems could show the location precisely, the recognition of abnormal cases does not result in decrease of the doctors' labor in the mass screenings.

DOI: 10.14738/jbemi.16.781
Publication Date: 29th December 2014
URL: http://dx.doi.org/10.14738/jbemi.16.781

Therefore, for the sake of reducing the labor by decreasing the number of the readings, a CAD for discriminating normal cases using digital gastric X-ray images was reported [6]. In the images of double contrast X-ray images of stomach, the folds appear in parallel on the stomach wall of normal cases. On the other hand, in abnormal cases, the folds just appear to be irregular in addition to cases where the folds concentrate at a spot. Hence, this system first extracts the folds in the stomach area of the images and then measures degrees of parallelism for the folds. The degrees are measured by extracting characteristics from distribution of the folds in 2D space. After that, using the features, this system discriminates normal cases using a classification machine. However, since the features were strongly depended on the size of stomach area, the system could not always recognize the normal cases correctly. In addition, the extraction of the folds were not automatic. Therefore, this paper proposes a method for extracting the folds automatically and improve the features for measuring the normality.

2 Double Contrast X-Ray Images of Stomach

In radiography to obtain contrast X-ray pictures of stomach, participants drink barium and radiologists take eight X-ray pictures changing direction of their body. Diagnosticians first choose the head-on double contrast X-ray picture among the eight pictures and diagnose the stomach reading it. When it is difficult to diagnose the stomach due to an uncertain stomach or a doubtful case, the other seven pictures are used as the second material. Therefore, as the first step for designing the CAD system of diagnosing normal cases of stomach, the head-on double contrast X-ray images are used throughout this paper. Figure 1 shows double contrast gastric X-ray pictures, where the left is a normal case and the right is an abnormal one. Both of them show folds inside the stomach area. As shown in the left image, folds appear like they are put side by side in parallel in normal cases. On the other hand, in the right image of an abnormal case, folds appear to be irregular. And, Figure 2 shows a typical pattern of gastric cancer, where the folds appear like lines concentration at a spot. The existing CAD systems find the location of gastric cancer such as this by recognizing the concentration pattern of lines in the images. After a lesion appear in the stomach area like gastric cancer or ulcer, the lesion part becomes hard on the gastric wall. Due to this phenomenon, folds are disordered around the part or in the whole of the gastric wall as shown in the right image in Figure 1. These stomachs such as Figure 1 (right) and 2 are diagnosed as abnormal case in mass screenings of gastric cancer and its carriers have to have a re-inspection by another way such as the photogastroscope.

Throughout this paper, all the double contrast X-ray pictures are digitalized as images by CR (Computed Radiography). The size of the images is 1024×1024 pixels with 256 gray levels.

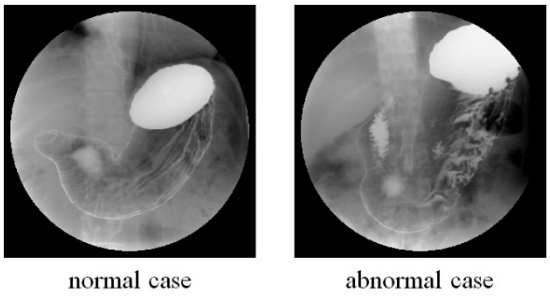

Figure 1: Double contrast X-ray images of stomach

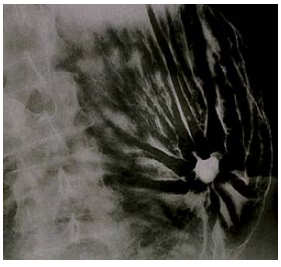

Figure 2: A concentration pattern of stomach folds (a typical case of gastric cancer)

3 Proposed Method

3.1 Preparation

As shown in Figure 1, to extract the characteristic of parallelism for the folds, a lot of noises such as the spinal column, unevenness density, etc. are existed in the images. Generally, in double contrast gastric X-ray images, since the contrast is weak and noises are much around the pyloric part, it would be difficult for even diagnosticians to read the part. To the contrary, since the contrast is strong around the cardia, the folds tend to appear clearly. Hence, as a preprocessing, the target area to extract the parallelism of folds is manually extracted as follows. First, using a tablet PC, a stomach area is extracted by roughly drawing its outline as shown in Figure 3(b). Next, the target area is extracted under the following conditions:

1) The area is the lower part from the horizontal line (b in Figure 3(c)) located at the bottom of the barium-pool, and

2) The area is the righter part from the vertical line (an in Figure 3(c)) located at the connection of the barium-pool to the left side edge in the cardia.

Besides, since the boundary of the stomach area becomes a noise for the extraction of folds, ten pixels from the right side of the boundary of the area to the inner of the area, and thirty pixels from the left side to the inner are cut at every row from the area. Similarly, two pixels from the upper boundary to the inner and ten pixels from the lower boundary to the inner are cut at every column, too. The last area is regarded as the target area. Figure 3 shows the extraction process of the target area, where A is the barium-pool, B is the cardia, C is the pylorus, and Figure 3(d) shows the target area R(x, y) for the image of Figure 3(a). The reason why the target area is restricted as shown above is because the folds appear clear and stable comparatively under the barium-pool, and noises such as shadows of other organs are roughly removed.

A method for extracting the whole stomach area based on the Snake algorism [7] was separately proposed for CAD systems of gastric cancer [8]. However, it is still necessary to enhance its quality for practical use. And, although the target area is extracted by hand as shown above, note that the region for the diagnosis in all the existing CAD systems was extracted manually as well. Therefore, an automated extraction of the target area is designed separately as a future work.

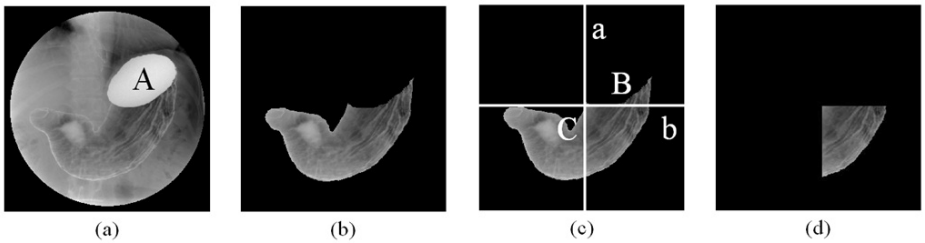

Figure 3: The target area for the normality extraction.

3.2 Extraction of the folds

In the X-ray images, pixel values of the folds are higher than other area and appear remarkably. Considering these characteristics, the brightness gradient strength F(x, y) and the pixel values H(x, y) which is output of the high-pass filter by 7x7 mask [9] are calculated to the target area R(x, y). F(x, y) is obtained by Eq.1. Next, in the 2D feature space created by F(x, y) and H(x, y), every pixel of the folds is classified by k-means clustering [10] into "a candidate of the fold area" and "others". When k-means clustering separates the pixels into two classes, two initial pixels have to be prepared. In this k-means clustering, the couple of two pixels which has the longest distance in the feature space are selected as the initial pixels. For example, after the k-means clustering is conducted to the image of Figure 4(a), the image is converted into Figure 4(b), where the white pixels represents the candidates. Thus, in outputs by the k-means clustering, we can see several regions are appeared. Finally, the folds are extracted by the linear discriminant analysis regarding perimeter of each candidate area as a variable of the discriminant analysis. The discriminant analysis is applied to every candidate area in the image and their discriminant score decides whether the candidate area belongs in the folds or its background. If the score for the region is more than 0, the region belongs in the folds. Figure 4(c) shows the folds extracted from Figure 4(a) via Figure 4 (b).

$$F(x,y)=\sqrt{F_x(x,y)^2+F_y(x,y)^2}$$
$$\begin{cases}F_x(x,y)=R(x+1,y)-R(x-1,y)\\F_y(x,y)=R(x,y+1)-R(x,y-1)\end{cases} \quad (1)$$

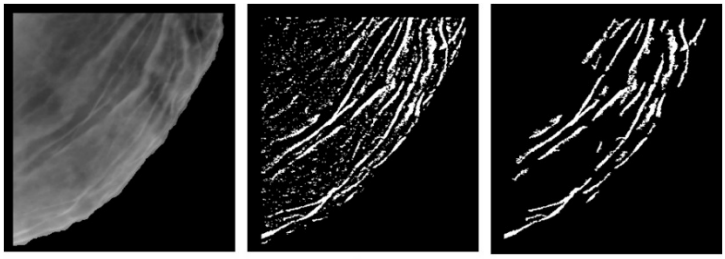

(a) (b) (c)

Figure 4: Process for extracting the folds.

3.3 Extraction of features

3.3.1 Extraction of the normalities: f1, and f2

First, the vector convergence index filter [11] is applied to the target area *R*(*x*, *y*). The filter outputs the value *ang*(*x*, *y*) of line angle at every pixel in *R*(*x*, *y*), where $0 \leqslant ang(x, y) < 180$. *AngSum* (*i*) is the number of pixels of the angle *i* in the folds, where $0 \leqslant i < 180$. Feature f_1 is defined as the kurtosis for *AngSum* (*i*).

$$f_1=\frac{1}{180}\sum_{i=0}^{179}\frac{(AngSum(i)-m)^4}{s^4} \quad (2)$$

Where, *m* is the mean value of *AngSum* (*i*) and s^2 is the variance of the *AngSum* (*i*). The folds' curves of normal cases appear in parallel along the outline of stomach area, i.e., shape of the curves depends on

the outline. Receiving this phenomenon, f_1 measures parallelism of the folds considering the outline of stomach area by extracting the kurtosis for the one dimensional array *AngSum*.

Next, when *AngSum* (*i_max*) is the maximum number among *AngSum* (0) – *AngSum* (179), regarding the angle *i_max* as *AngMax*, feature f_2 is defined as the proportion of the folds around *AngMax* (*AngMax*$\pm$ 12) to all the folds.

$$f_2 = \frac{1}{area}\sum_{i=0}^{179} F(i)$$
$$F(i) = \begin{cases} AngSum(i), & if\ \ AngMax - 12 \le i, and\ i \le AngMax + 12 \\ 0, & otherwise \end{cases} \quad (3)$$

Where *area* is the number of pixels in the folds, f_2 represents degree of unity for directions of the folds' curve. Since the folds figure with parallel curves in the target area of normal cases, the directions would be concentrated in a small range of angle.

3.3.2 Extraction of the normality: f3

Since folds appear irregularly in abnormal cases and intervals between the folds are smaller than normal cases, the intersections of the folds are much and crowd in zones (which could be lesions) than normal cases. To catch the characteristic, first, the thinning is conducted to the folds. And then, the number of pixels which have are the intersection of at least three neighbors in 8-neighbor are extracted. After that, the folds are removed within the radius *r* at every intersection. Feature f_3 is defined as the proportion of the sum of folds which remained after the folds' removal in the circle of every radius *r* to all the folds.

$$f_3 = \frac{1}{area}\sum_{r=1}^{Rmax} number(r) \quad (4)$$

where *area* is the number of pixels in all the folds, *Rmax* is the radius in the case when all the folds are removed from the target area, and *number*(*r*) is the number of pixels which represent the remained folds in the target area when the removal is conducted within the circle of the radius *r*. f_3 represents the content of the folds which figure parallel curves to all the folds. In normal cases of the X ray images, since the folds figure parallel curves and crossed curves are hardly perceived, the content in the normal cases could be much than abnormal cases.

Figure 5 shows an extraction result of the intersections, where (a) is the folds, (b) is the thinning for the folds, and (c) is the intersections.

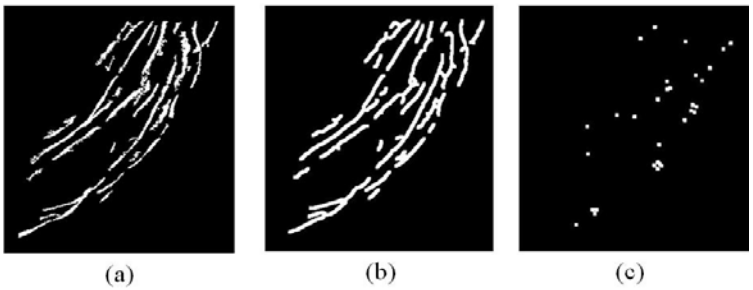

Figure 5: Process for extracting the intersections.

4 Experimental Results

The proposed normalities were extracted from 88 X-ray images (normal case: 75, abnormal case: 13). To examine performance of the proposed normalities, linear discriminant analysis (LDA), linear support vector machine (L-SVM), and nonlinear support vector machine (N-SVM) were applied to the discrimination of the images into normal or abnormal cases by regarding the normalities as variables, respectively. Each of the normalities was normalized to the dataset that the mean value is 0 and the variance is 1. As a kernel function in N-SVM, the Gaussian kernel was used.

The training dataset and test dataset were chosen by the leave-one-out cross validation [12] in all the discriminations. In fact, every discrimination was conducted according to the following procedure:

1. Choose 1 image from all the images as test data, and use the other images as training dataset.
2. Discriminate the test data between the class of "normal" and "abnormal".
3. Changing the test data, repeat from 1 to 2 until every image has been the test data.

4.1 The discrimination of the normal cases including synthetic samples

Performance of machine learning algorithms is typically evaluated using predictive accuracy. However, this is not appropriate when the data is imbalanced and/or the costs of different errors vary markedly. The machine learning community has addressed the issue of class imbalance in two ways: the one is to assign distinct costs to training examples, and another one is to re-sample the original dataset, either by over-sampling the minority class and/or under-sampling the majority class. Here, we apply over-sampling of the minority class (i.e., the class of abnormal cases) using SMOTE [13].

SMOTE is over-sampled by creating "synthetic" examples rather than by over-sampling with replacement. This method creates extra training data by performing certain operations on real data. Synthetic examples are generated in a less application-specific manner by operating in the feature space. The synthetic samples are generated in the following way: Take the difference between the feature vector (sample) under consideration and its nearest neighbor. Multiply this difference by a random number between 0 and 1, and add it to the feature vector under consideration. This causes the selection of a random point along the line segment between two specific features. This approach effectively forces the decision region of the minority class to become more general.

We prepared 75 samples in the normal cases and 75 (i.e. 13 real + 62 synthetic samples) samples in the abnormal cases for the training set used in the leave-one-out cross-validation. The class of abnormal cases was oversampled at 478% of its original size. Table 1 shows discrimination results for normal and abnormal cases respectively obtained by the three discrimination machines of LDA, L-SVM and N-SVM (σ=1.0), where *Precision* and *Recall* represent the discrimination ratio. They are defined as

$$Precision = \frac{X_{h\cap c}}{X_c} \times 100 \tag{5}$$

$$Recall = \frac{X_{h\cap c}}{X_h} \times 100 \tag{6}$$

Where X represents the number of images, X_h is the number of the correct answers, and X_c is the number of images discriminated by the proposed method. Figure 6 shows the discrimination ratios

against change of the parameter σ in the Gaussian kernel used in N-SVM. Table 2 shows the discrimination ratios in the case when the discrimination by N-SVM have shown the highest performance (σ = 0.4).

Table 1: Experimental results including synthetic abnormal samples.

	Normal		Abnormal	
Tool	*Recall*	*Precision*	*Recall*	*Precision*
LDA	81.33% (61/75)	100% (61/61)	100% (75/75)	84.26% (75/89)
L-SVM	85.33% (64/75)	100% (64/64)	100% (75/75)	87.20% (75/86)
N-SVM (σ =1.0)	88.00% (66/75)	100% (66/66)	100% (75/75)	89.28% (75/84)

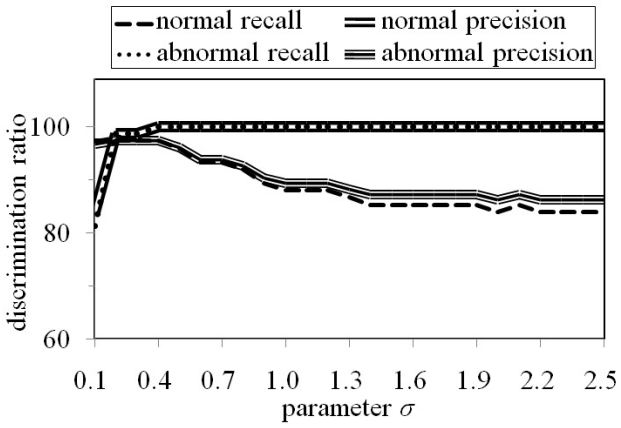

Figure 6: The discrimination ratio vs. σ of the Gaussian kernel in N-SVM.

Table 2: Experimental result in the case when σ = 0.4 in N-SVM.

	Normal		Abnormal	
Tool	*Recall*	*Precision*	*Recall*	*Precision*
N-SVM (σ =0.4)	97.33% (73/75)	100% (61/61)	100% (75/75)	97.40% (75/77)

As shown in Table 1 and Figure 6, the discrimination ratios for each of normal and abnormal cases show more than 80 % and the *Precision* of the normal cases keeps 100 %. Actually, in order to pass the reading test of mammography images in Japan, medical doctors have to correctly read at least 80 % in each of cancer cases and normal cases. Hence, if the experimental results were evaluated from this clinical standpoint, the experimental results would show the proposed normalities are appropriately extracted for the discrimination of normal cases in the gastric X-ray images.

4.2 The discrimination of the normal cases only real samples

Using 75 cases in the normal cases and 13 cases in the abnormal cases (without the over-sampling in 4.1), the discriminations were conducted by the leave-one-out cross-validation as well as 4.1. Table 3 shows discrimination results for normal and abnormal cases respectively obtained by the three discrimination machines of LDA, L-SVM and N-SVM (Gaussian kernel, σ=1.0), where *Precision* and *Recall*

represent the discrimination ratio. Table 4 shows the mean value and the standard deviation of each normality extracted from correct dataset in each case. As shown in Table 4, we can confirm that all the normalities for the normal cases are higher than the abnormal cases.

Table 3: Experimental results using clinical cases.

	Normal		Abnormal	
Tool	*Recall*	*Precision*	*Recall*	*Precision*
LDA	78.66% (59/75)	100% (59/59)	100% (13/13)	44.82% (13/29)
L-SVM	85.33% (64/75)	100% (64/64)	100% (13/13)	51.16% (13/24)
N-SVM (σ=1.0)	86.66% (65/75)	100% (65/65)	100% (13/13)	56.52% (13/23)

Table 4: Results of the extraction of the normalities.

	Normal		Abnormal	
Normality	*Mean*	*SD*	*Mean*	*SD*
f_1	0.109	1.043	-0.632	0.325
f_2	0.178	0.977	-1.027	0.310
f_3	0.206	0.935	-1.193	0.353

Figure 7 shows the result of the extracted folds and intersections for a normal case of discrimination success, where (a) is the target area, (b) is the folds, and (c) is the intersections. Similarly, Figure 8 shows the result for an abnormal case of discrimination success.

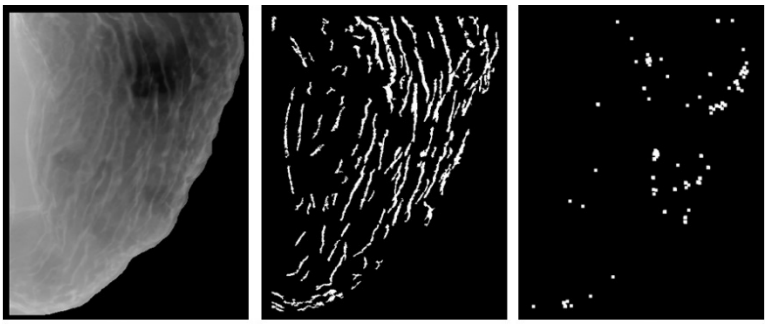

Figure 7: A result of the extracted folds and intersections for a normal case (discrimination success).

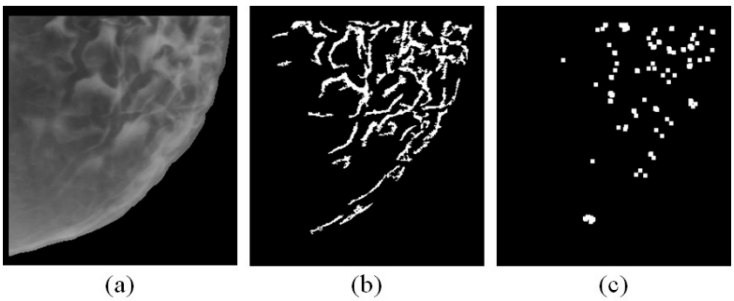

Figure 8: A result of the extracted folds and intersections for an abnormal case (discrimination success).

5 Discussions

In the experimental results, 8 normal cases were diagnosed as abnormal cases in all the discrimination machines. They can be broadly divided into two kinds. Figure 9 and Figure 10 show a case of each kind, where (a), (b) and (c) are the same as Figure 7, respectively.

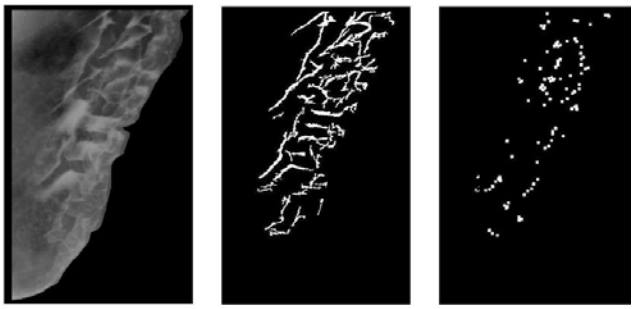

Figure 9: Failure case 1 (by the proposal: abnormal, correct answer: normal)

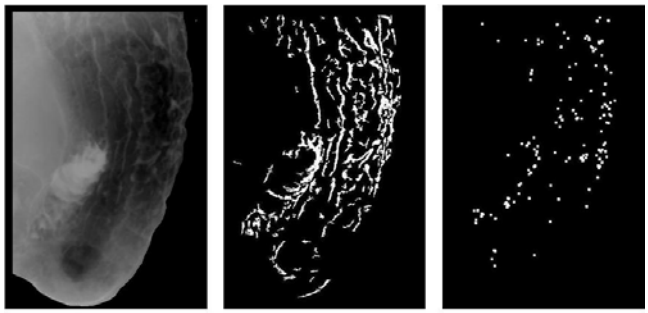

Figure 10: Failure case 2 (by the proposal: abnormal, correct answer: normal)

In the case of Figure 9, the folds could look irregular though this case is a normal case. Besides, the normalities for this case are f_1 = -0.397, f_2 = -0.659 and f_3 = -1.290, i.e., the normalities are closer to the mean value of them in abnormal case shown in Table 3. The reason why the discrimination result of this case is opposite to the diagnosis by a medical doctor is because medical doctors imagines the stomach in the images as a 3D stomach based on their past experience, i.e., they can imagine the depth of the stomach from the X-ray image. On the other hand, in the proposed method, the normalities cannot be extracted by considering the depth of the stomach from the X-ray images. Since the stomach repeats the expansion and contraction contracted movement, there are some cases of stomachs which show distorted wall or have thicker pleats on the wall (i.e., shadow of the folds is thicker and stronger than other cases) in the X-ray images. However, the normalities are not precisely extracted from such cases because all the stomachs are not recognized as a 3D object. In the future, it is necessary to improve the normalities or propose another normality considering the depth between folds in the target area. The other 4 normal cases were discriminated incorrectly for the same reason.

In the case of Figure 10, we can confirm the leakage of barium in the intestine. Since the proposed method cannot distinguish between the folds and the noises, the proposed method cannot extract the features precisely such cases. In the image shown in Figure 10, f_1, f_2 and f_3 are -0.914, -1.086 and -0.609, respectively, and they are closer to the mean values of them in abnormal case than normal case shown

in Table 3. The other 2 normal cases were discriminated incorrectly for the same reason. In the future, it is necessary to consider recognizing the leakage in the target area.

6 Conclusions

Aiming at decreasing the number of gastric X-ray pictures which diagnosticians have to read at a time, this paper has presented features for discriminating normal cases from gastric abnormal cases. The characteristic of the features is to measure the normality of fold patterns in double contrast X-ray images of stomach. The features were used as variables of discrimination machines to identify normal cases. Experimental results by the discrimination trials have shown that discrimination ratios of normal cases by the proposed method have become more than 80% in all the trials.

As future works, it would be necessary to (1) extract the target area automatically, (2) design normalities for the diagnosis considering the depth of stomach in the X-ray images, and (3) remove region of the leakage of barium in the target area.

REFERENCES

[1]. Y. Kita (1996), 'Elastic-model driven analysis of several views of a deformable cylindrical object', IEEE Trans. Pattern Anal. Mach. Intel., 18(12), 1150-1162.

[2]. Y. Mekada, J. Hasegawa, J. Toriwaki, S. Nawano, and K. Miyagawa (1998), 'Automated extraction of cancer lesions from double contrast X-ray images of stomach', Proc. 1st International Workshop on Computer Aided Diagnosis, 407-412.

[3]. J. Hasegawa, T. Tsutsui, and J. Toriwaki (1991), 'Automated Extraction of Cancer Lesions with Convergent Fold Patterns in Double Contrast X-ray Images of the Stomach', Systems and Computers in Japan, 22(7), 51-62.

[4]. J. Hasegawa and J. Toriwaki (1992), 'A new filter for feature extraction of line pattern texture with application to cancer detection', Proc. 11th IAPR Int. Conf. on Pattern Recognition, 352-355.

[5]. Y. Yoshinaga, H. Kobatake, and S. Fukushima (1999), 'The detection and feature extraction method of curvilinear convex regions with weak contrast using a gradient distribution method', Proc. IEEE ICIP 99, 715-719.

[6]. K. Abe, T. Nobuoka, and M. Minami (2011), 'Computer-Aided Diagnosis of Mass Screenings for Gastric Cancer Using Double Contrast X-ray Images', Proc. IEEE Pacific Rim Conf. on Communications, Computers and Signal Processing, 708-713.

[7]. M. Kass, A. Witkin, and D. Terzopoulos (1988), 'Snakes: Active contour models', Int. J. Computer Vision, 1(3), 321-331.

[8]. S. Fukushima, H. Uwai, and K. Yoshimoto (2000), 'Optimization-Based Recognition the Gastric Region from a Double-Contrast Radiogram', IEICE Trans. (Japanese Edition), J83-D-II (1), 154-164.

[9]. R. A. Schowengerdt (1983), 'Techniques for Image Processing and Classfication in Remote Sensing', ACADEMIC PRESS, 72-83.

[10]. M. J. Canty (2014), 'Image Analysis, Classification and Change Detection in Remote Sensing', CRC Press, 329-332.

[11]. Y. Yoshinaga and H. Kobatake (2000), 'The line detection method with robustness against contrast and width variation applied in gradient vector field', Systems and Computers in Japan, 31(3), 49-58.

[12]. M. Stone (1974), 'Cross-Validatory Choice and Assessment of Statistical Predictions', J. of the Royal Statistical Society, Series B (Methodological), 36(2), 111-147.

[13]. NV. Chawla, KW. Bowyer, LO. Hall, and WP. Kegelmeyear (2002), 'SMOTE: Synthetic Minority Over-sampling Technique', J. of Artificial Intelligence Research 16, 321-357.

SOCIETY FOR SCIENCE AND EDUCATION UNITED KINGDOM

JBEMi JOURNAL OF BIOMEDICAL ENGINEERING AND MEDICAL IMAGING

ISSN: 2055-1266
VOLUME 1, ISSUE 6

Identifying the Muscle Synergy Pattern during Human Grasping

[1]Afsaneh Koohestani, [2]Hamid Reza Kobravi and [3]Mahereh koohestani
Islamic Azad University of Mashhad, Iran & the Institute of training, research, healthcare of Ghaem, Iran
[1]afsaneh_koohestani@ymail.com; [2]hkobravi@gmail.com; [3]mahereh.koohestani@gmail.com

ABSTRACT

In this work, a methodology has been proposed and evaluated for identification the muscle synergy patterns during human grasping. The proposed approach is based on decomposition analysis of involved muscle activation profiles utilizing the Hierarchical Alternating Least Squares (HALS) algorithm. The surface EMG signals of Flexor Digital Superfacialis and Flexor Pollicis Longus muscles were recorded during grasping a cylindrical object. EMG signals were full-wave rectified and smoothed through a low pass filter. Then the HALS algorithm was utilized for decomposition of muscle activation profiles. The HALS algorithm can be efficiently used instead of NNMF (non-negative matrix factorization) method. The HALS method not only provides a very good convergence property but also there is not the non-negativity constraint for the decomposed factors. The results of evaluations are interesting and promising.

Key words: Surface EMG, Hals algorithm, muscle synergy

1 Introduction

A functional muscle synergy means the pattern of co-activation of muscles recruited by a single neural command signal [2]. The central nervous system (CNS) uses multiple joints and muscles to perform the stable and flexible goal-directed movements. Existence of muscle synergies as a neural strategy has been proposed to justify how the CNS can solve the problem of redundancy and how it copes with complexity of control problem [1,7and13].

In recent years, many evidences have been presented proving modularity during the performance of different motor tasks in humans and other animals [3, 4]. According to modular control hypotheses, the motor primitives that are organized at the spinal level are modules that in a linear or non-linear manner can be combined to produce enormous collection of movements [2]. Muscle synergies are the possible candidates for motor primitives [10]. It is also has been shown that the decomposition of EMG envelope can be resulted in identifying a small number of muscle synergies [7, 14]. There are two main models for muscle synergies called synchronous muscle synergies and asynchronous muscle synergies [7, 8, and 9].

Recently, Castellini et al. [6], have presented the evidences of synchronous muscle synergies during human grasping using Principal Component Analysis (PCA). In this paper, we focused on human hand grasping while the wrist joint is at rest position. We analyzed the recorded SEMG signals of two muscles being involved in grasping a cylindrical object. We used NNMF method for EMG decomposition. Because it does not impose orthogonally and statistical independence (such as PCA and ICA respectively) [8,9]

DOI: 10.14738/jbemi.16.779
Publication Date: 30th December 2014
URL: http://dx.doi.org/10.14738/jbemi.16.779

and it seems more suitable for extracting the entire muscle synergies[5]. Nevertheless, the standard NNMF applies non-negativity constraint for the decomposed factors. Since, smoothed full-rectified EMG are used for decomposition, the modified EMG may has the negative values for no ideality of smoothing filters. So, in this paper, the HALS algorithm has been used instead of NNMF method [12]. The HALS method dose not applies such constraint. In addition, using The HALS results in achievement both better accuracy and repeatability [11].

The archived results show the acceptable performance of proposed methodology.

2 Method and Materials

2.1 Muscle synergy model

In the synchronous synergy model, the EMG can be decomposed as a linear combination of set of vectors capturing a specific balance of muscle activations [7], by a time-variant activation coefficient.

$$M(t) = \sum_{i=1}^{k} c_i \overrightarrow{(t).w_i} \quad (1)$$

M Represent the time-varying muscle activation pattern of d involved muscles. $\overrightarrow{w_i}$ is the ith d-dimensional basis vector. $c_i \overrightarrow{(t)}_i$, is the scalar activation coefficient for the ith basis vector.

In fact, each $\vec{w}_i$ represents a muscle synergy related to the synaptic weights from premotor neurons to different motor neuronal pools, each c_i represents the synergy activation coefficient or firing frequency recruiting a synergy.

2.1.1 Non-Negative Matrix Factorization

Most non-negative matrix decomposition methods are attributed to researchers such as Lee a Seung in which is the observation matrix [13]. Let's suppose:

$$M = C_{\pm} W_{\pm} + E \quad (2)$$

$$W = [w1, w2, \dots wj] \in R_{+}^{I \times T} \quad (3)$$

$$C = [c1, c2, \dots, cj] \in R_{+}^{I \times T} \quad (4)$$

Where W and C are matrices containing the basis vectors and activation coefficients and E represents estimation error.

Let's define a cost function for a w_j and its corresponding coefficient c_j using the Frobenius norm as bellows:

$$D_F^j(M^j || c_j w_j) = \frac{1}{2} ||M^j - c_j w_j||_F^2 \quad (5)$$

2.2 HALS Algorithm

In this manner we will have a bank of local cost functions. By minimizing the cost functions consecutively, based on the optimality conditions (KTT) [12], the stationary points of local cost function can be estimated using the gradient of local cost functions as follows:

$$\nabla_{c_j} D_F^j(M^{(j)}||c_j w_j^T) \geq 0 \quad (6)$$

$$\nabla_{w_j} D_F^j(M^{(j)}||c_j w_j^T) \geq 0 \quad (7)$$

Where the gradient of the local cost function can be estimated as follows:

$$\nabla_{c_j} D_F^j(M^j||c_j w_j) = \frac{\partial D_F^j(M^j||c_j w_j)}{\partial c_j} = c_j w_j^T c_j - M^j w_j \quad (8)$$

$$\nabla_{w_j} D_F^j(M^j||c_j w_j) = \frac{\partial D_F^j(M^j||c_j w_j)}{\partial w_j} = c_j^T c_j w_j - M^j c_j \quad (9)$$

If it is assumed the cj and wj are positive number then the stationary points can be estimated using the update laws as follows:

$$w_j \leftarrow \frac{1}{c_j^T c_j}\left[M^{j^T} a_j\right]_+ = \frac{1}{c_j^T c_j}\max\{\varepsilon, M^j w_j\} \quad (10)$$

$$w_j \leftarrow \frac{1}{c_j^T c_j}\left[M^{j^T} a_j\right]_+ = \frac{1}{c_j^T c_j}\max\{\varepsilon, M^j w_j\} \quad (11)$$

Where ε is a small positive number, above update rules are known as the HALS algorithm was proposed by Chikoki et al. [14].

2.3 Data Collection and Preprocessing

Ten healthy participants, men and women, are asked to hold a one-kilogram cylinder in their hands for 10 seconds and then drop it, and repeated it again for five times. During the experiments the wrist joint of the participants were at the rest posture. The recorded EMG signals was rectified and passed through a low-pass filter with 20 Hz cut-off frequency. Then, the obtained signals were normalized.

3 Results

One of most prevalent methods being used to determine the number of synergies is based on R2 criterion. R2 represents the fraction of total variation accounted for by the synergy reconstruction (Eq. 12), [15].

$$R^2 = 1 - \frac{SSE}{SST} = 1 - \frac{\sum_s \sum_{k=1}^{k_j} ||m^j(t_k) - \sum_i c_i^j w_i\left(t_k - t_i^j\right)||^2}{\sum_s \sum_{k=1}^{k_j} ||m^s(t_k) - \bar{m}||^2} \quad (12)$$

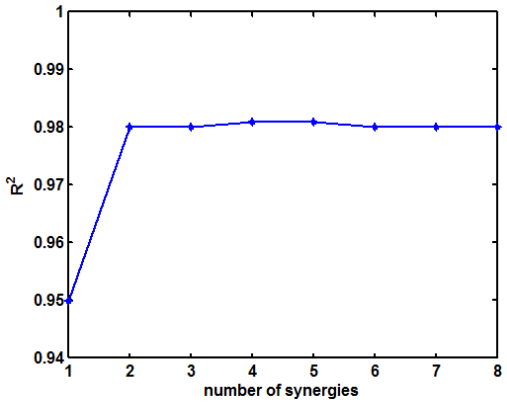

Figure 1: R2 changes versus the number of synergies.

Where *SSE* is the sum of the squared residuals, *SST* is the sum of the squared residual from the mean activation vector ($\bar{m}$). As the Fig.1 indicates, the slope of $\mathbf{R}^2$ changes has been decreased considerably at 2. So, in this work the number of selected synergies is 2.

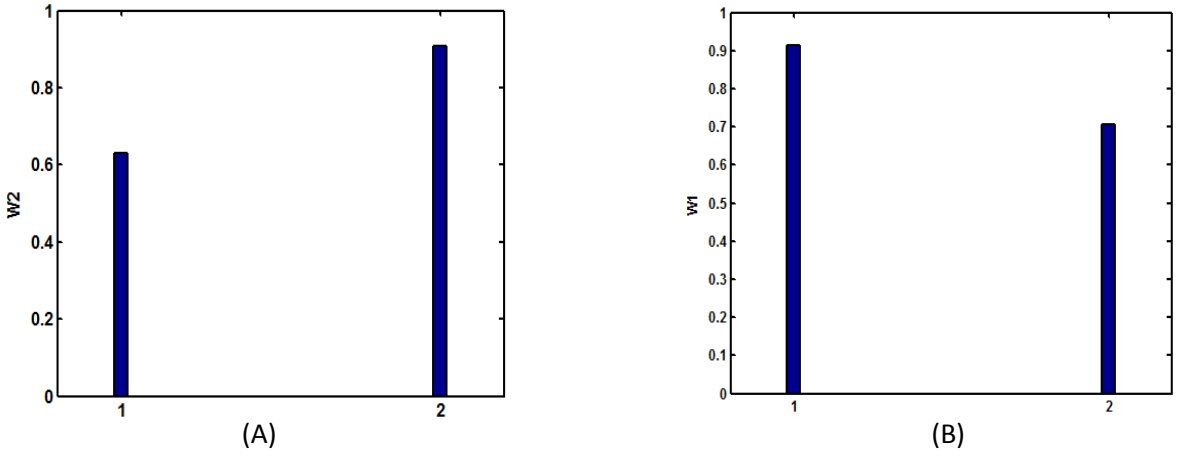

Figure 2: Shows the activation level of the two involved muscles corresponding to each synergy pattern

In the next step, basis vectors and activation coefficients were estimated using HALS algorithm described in the previous section. Figure 2, shows the activation level of the two involved muscles corresponding to each synergy pattern.

4 Discussion

In figure 3, the muscle synergy pattern during object grasping was extracted using analyses of computed muscle activation profiles relating to two involved muscles. In this research, HALS algorithm and NNMF were utilized for identifying the synergy vectors.

HALS algorithm is known as a fast convergent approach without non-negativity constraint for the decomposed factors [11, 14]. In the other hand, the main purpose of the present study was to achieve the proper muscle synergy patterns by solving the problem of nonnegative matrix analysis. For quantitative evaluation of the propose approach, the root mean square (RMS) of the error signal, the difference between the reconstructed muscle activation profiles and actual activation profiles, were calculated [Table 1]. The calculations show the low difference between the actual and reconstructed signals. This can be due to the efficiency of HALS algorithm; however there is difference between actual signal and reconstructed signal by NNMF algorithm.

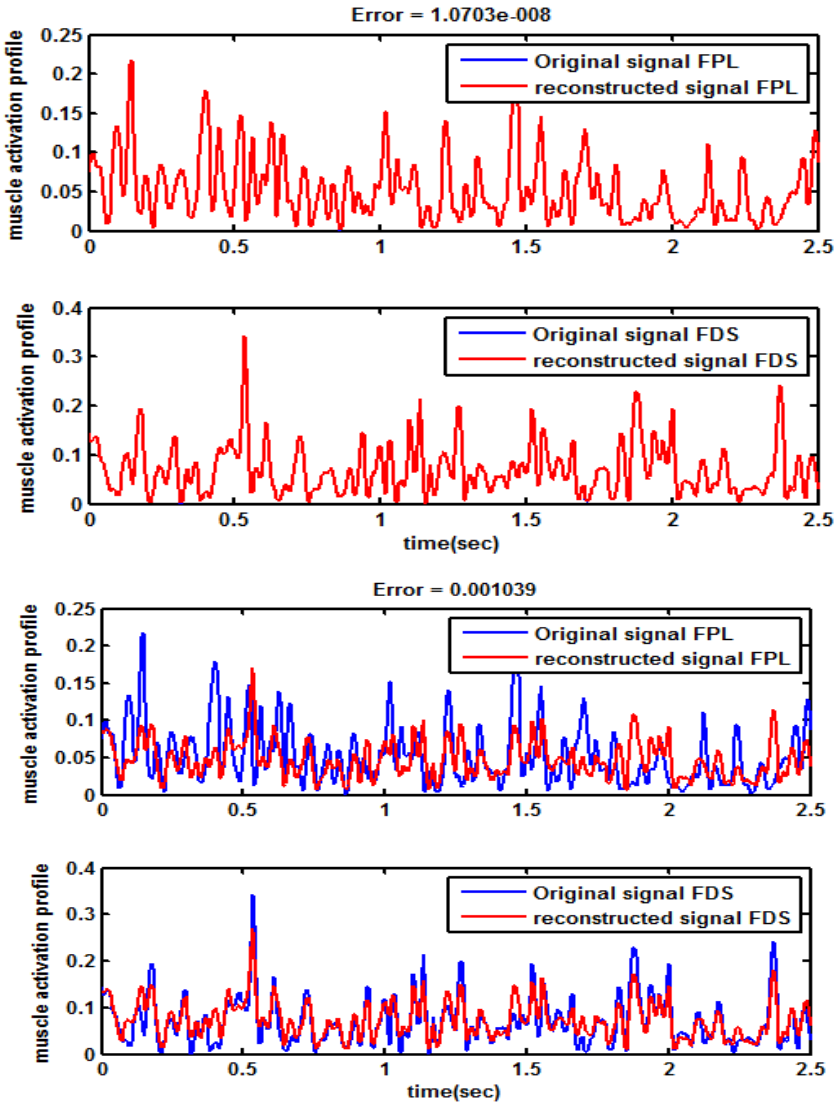

Figure 3: Comparing the reconstructed muscle activation with the original signals by 3 numbers of synergy, (A) demonstrate HALS algorithm and (B) demonstrate NNMF. FDS: demonstrates signals of Flexor Digital Superfacialis, FPL: demonstrates signals of Flexor Pollicis Longus

Table 1: Demonstrate RMS of both algorithm (Hals, NNMF) for Flexor Digital Superfacialis, Flexor Pollicis Longus

Subject	Rms(Hals) FDS$\times 10^{-8}$	Rms(Hals) FPL$\times 10^{-8}$	Rms(NNMF) FDS$\times 10^{-4}$	Rms(NNMF) FPL$\times 10^{-4}$
Male1	1.1511	1.2334	2.3647	2.2103
Male2	1.4567	1.9712	2.1999	2.3614
Male3	1.8835	1.3451	3.8041	3.1200
Male4	1.3260	1.0241	2.3330	2.3212
Male5	1.1249	1.7503	3.0100	3.0144
Female1	1.0241	1.0021	2.4851	2.4851
Female2	1.7503	2.0144	3.3541	3.3541
Female3	1.0021	1.0222	3.0144	1.0039
Female4	2.0006	2.0314	1.4729	3.1533
Female5	1.0703	1.3766	2.0342	2.0342

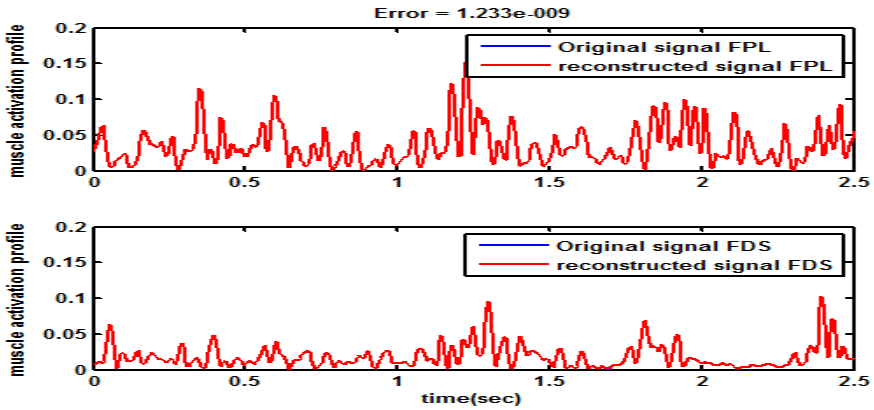

Figure 4: Comparing the reconstructed muscle activation with the original signals by 2 numbers of synergy, HALS algorithm

If number of synergies over estimated, we are going to compare the performance of reconstruction method base on HALS algorithm.

In figure.4, showed that when the number of synergies are over estimated (more than 2 synergies), there was not seen any difference between the actual signal and reconstructed signal. After identifying the synergy vectors, the activation profile of two involved muscles were reconstructed using the estimated basis vectors and coefficients. The reconstructed profiles were compared to the actual activation profiles. Figure 3, 4 and table 1, show reconstructed muscle activation profiles, computed, accompanied by actual computed muscle activation profiles. This research illustrated for the first time, it could be reconstructed signals by the minimizing of the number of synergies like 2 synergies.

Identifying the muscle synergy patterns, quantifying the modular organization of motor control, can provide insights on novel diagnostic and rehabilitation tools [11]. The achieved results prove the presented method has potential application to the neuron- rehabilitation.

5 Result

Difference between the reconstructed muscle activation profiles and actual activation profiles, were calculated for ten participants in hand grasping. The calculations showed the low difference between the actual and reconstructed signals. This can be due to the efficiency of HALS algorithm.

ACKNOWLEDGMENT

This work was supported by Neuromuscular Control Lab, biomedical department, Islamic Azad University, Mashhad branch, and also supported by physiotherapy department, Ghaem hospital, Mashhad University of Medical Sciences.

REFERENCES

[1] M. C. Tresch and A. Jarc,. “The case for and against muscle synergies”. Current Opinion in Neurobiology”.19, 601-607, 2009.

[2] Bernstein, N. "The coordination and regulation of movements". Pergamon Press, Oxford.1967.

[3] Lacquaniti, F., Ivanenko, Y.P., Zago, M. "Patterned control of human locomotion". J. Physiol. 590, 2189–2199 .2012.

[4] Bizzi, E., Cheung, V.C., d'Avella, A., Saltiel, P., Tresch, M. "Combining modules for movement". Brain Res. Rev. 57, 125–133. 2008.

[5] D. Ioannis, B. Bastien, P. Thierry and P. Stefano, "A methodology for assessing the effect of correlations among muscle synergy activations on task-discriminating information", Frontiers in Computational Neuroscience, 7, 2013, Article 54.

[6] Castellini, C., van der Smagt, P. "Preliminary evidence of dynamic muscular synergies in human grasping". In: Proceedings of ICAR -International Conference on Advanced Robotics, 28-33 (2011).

[7] A. d'Avella, P. Saltiel and E. Bizzi, "Combinations of muscle synergies in the construction of a natural motor behavior", Nat Neurosci, 6, 300–308. 2003.

[8] L. Omlor and M. A. Giese, "Anechoic blind source separation using wigner marginal" J. Mach. Learn.Res., 12, 2011, 1111–1148.2011

[9] A. d'Avella, L. Fernandez, A. Portone and F. Lacquaniti, "Modulation of phasic and tonic muscle synergies with reaching direction and speed", J. Neurophysiol, 100, 1433–1454, 2008.

[10] E. Bizzi, A. D'Vella, P. Saltiel and M. Tresch, "Modular organization of spinal motor systems", Neuroscientist, 8,437–442, 2002.

[11] A. H. Phan and A. Cichocki, "Multi-way nonnegative tensor factorization using fast hierarchical alternating least squares algorithm (HALS)", In Proc. of the 2008 International Symposium on Nonlinear Theory and its Applications, Budapest, Hungary, 2008.

[12] Cichocki, A., Zdunek, R., & Amari, S. I., "Hierarchical ALS Algorithms for Nonnegative Matrix and 3D Tensor Factorization", in ICA07, London, UK, September 9-12, Lecture Notes in Computer Science, 2007,4666, pp. 169-176.2007.

[13] Lee, D. D., & Seung, H. S., "Algorithms for Nonnegative Matrix Factorization", Advances in neural information processing systems, 13, 556-562,2001.

[14] A. Cichocki, R. Zdunek, A. H. Phan and S. Amari, "Nonnegative Matrix and Tensor Factorizations", John Wiley & Sons Ltd: Chichester, UK, 2009.

[15] Andrea d'Avella, Alessandro Portone, Laure Fernandez and Francesco Lacquaniti, "Control of fast-reaching Movements by Muscle synergy combinations. J.Neuroscience, 26,77917810, 200

SOCIETY FOR SCIENCE AND EDUCATION UNITED KINGDOM

JBEMi JOURNAL OF BIOMEDICAL ENGINEERING AND MEDICAL IMAGING

ISSN: 2055-1266
VOLUME 1, ISSUE 6

A Fuzzy Set Approach to Bacterial Wilt Recognition

[1]Obi J.C., [2]Imianvan A.A. and [3]Okpor D.M

[1&2]Department of Computer Science, University of Benin, Benin City, Nigeria.

[3]Department of Computer Science, Delta State, Polytechnic, Ozoro, Nigeria

[1]tripplejo2k2@yahoo.com, [2]tonyvanni@yahoo.com,[3]magaretokpor20@yahoo.com

ABSTRACT

Bacterial wilt (Ralstonia Solanacearum) is a bacterial which attack most plant species in different plant families resulting in numerous financial implications to farmers. The predominant symptoms includes: yellowish leaves, permanent wilted leaves, permanent upright leaves, brownish vascular tissues, dark brownish cortex and thin thread of ooze infected structure. Bacterial wilt can be readily spread through the movement of contaminated soil and infected vegetative propagated plants, in contaminated irrigation water, and on the surfaces of tools (cutting knives) and equipment used to work with the plants, and on soiled clothing. It often attacks many floricultural and vegetable bedding plant crops. Some of the other known hosts of bacterial wilt include Pelargonium, tomato, peppers, eggplant, bean, and beet. Most of the approaches for bacterial wilt recognition are quite time consuming and subjective in nature. Therefore we proposed an objective approach, capable of initiating fuzzy rules with the aim of quick and objective recognition of bacterial wilt attack.

Keywords: Bacterial wilt, Fuzzy classifier, Fuzzy logic, Inference Rules, Set theory

1 Introduction

Bacteria called Ralstonia Solanacearum (bacterial wilt) attack almost 200 plant species in 33 different plant families (Gary, 2014). This constitutes one of the largest known host ranges for any plant pathogenic bacterium. In tobacco, it is called bacterial wilt, Granville wilt, Moko disease, southern wilt or southern bacterial wilt (Jones, 1993). This bacterium is noted for diseases caused outdoors in land areas bounded by 45N and 45S latitudes where rainfall averages above 100 cm/year (39 in/year), the average growing season exceeds 6 months, the average winter temperatures are not below 10°C (50°F), the average summer temperatures are not below 21°C (70°F) and the average yearly temperature does not exceed 23°C (72°F) (Kim et al., 2003). It can be moved from such areas into the greenhouse industry in and on plants propagated in those regions and then sold to growers throughout the world. Although the primary location of survival in the environment is in crop and weed hosts, it can also survive in soil. It can be readily spread through the movement of contaminated soil and infected vegetative propagated plants, in contaminated irrigation water, and on the surfaces of tools (cutting knives) and equipment used to work with the plants, and on soiled clothing (Gary, 2014).

The bacteria were first named Bacillus solanacearum. After several revisions, it was called for many years Pseudomonas solanacearum (Kim et al, 2003). The latest revision has settled on the name

DOI: 10.14738/jbemi.16.761
Publication Date: 1st January 2015
URL: http://dx.doi.org/10.14738/jbemi.16.761

Ralstonia solanacearum (Jones, 1993; Kim et al., 2003). It is described as a non-spore forming, gram negative staining, nitrate-reducing, ammonia-forming, aerobic, rod-shaped (0.5-1.5 µm) bacteria with one polar flagellum. Populations within this genus and species can be further divided into races and biovars based on differing host ranges, biochemical properties, susceptibility to bacteria-infecting viruses (phages), and serological reactions. It attacks many floricultural and vegetable bedding plant crops including geraniums (all Pelargonium), Catharanthus, Impatiens, Ageratum, Chrysanthemum, Gerbera, Tagetes, Zinnia, Salvia, Capsicum, Lycopersicon, Nicotiana, Petunia, Solanum melongena (eggplant), Tropaeolum (nasturtium) and Verbena (Jones, 1993; Kim et al., 2003). Some of the other known hosts include Pelargonium, tomato, peppers, eggplant, bean, and beet. Weed hosts include black nightshade, climbing nightshade, horsenettle, Jimson weed, purslane, mustards, lambs-quarters, and bitter-gourd. The bacteria can infect through roots and through any fresh wounds. The bacterium can be difficult to work with in the laboratory because it quickly loses pathogenicity and viability in artificial. The symptoms of bacterial wilt includes; yellowish leaves, permanent wilted leaves, permanent upright leaves, brownish vascular tissues, dark brownish cortex and thin thread of ooze infected structure.

The focal point of this paper centres on recognizing bacterial wilt utilizing an objective fuzzy set theory (union) approach. Fuzzy Logic provides a means of representing and manipulating data that are not precise, but rather fuzzy. The theory of fuzzy logic utilizes mathematical strength to capture the uncertainties associated with human cognitive processes. Existing methods (traditional or conventional) for analysing (test data) of bacterial wilt uses approaches (techniques) that are unable to handle uncertain or vague data. In this paper, the rich facilities of fuzzy classifier is utilize for dealing with such uncertainties.

2 Material and Method

A Fuzzy classifier is an algorithm that assigns a class label to an object, based on the object description. It is also said that the classifier predicts the class label (Angelov and Zhou, 2008). The object description comes in the form of a vector containing values of the features (attributes) deemed to be relevant for the classification task (Ishibuchi et al., 1995). Typically, the classifier learns to predict class labels using a training algorithm and a training data set. When a training data set is not available, a classifier can be designed from prior knowledge and expertise. Once trained, the classifier is ready for operation on unseen objects (Cordon et al., 1999). Classification belongs to the general area of pattern recognition and machine learning (Babuska, 1998). The attributes includes:

a. Soft labelling. The standard assumption in pattern recognition is that the classes are mutually exclusive. This may not always be the case. A standard classifier will assign a single crisp label. A fuzzy classifier can assign degrees of membership (soft labels). A standard classifier can output posterior probabilities, and offer soft labeling too. A fuzzy classifier, D, producing soft labels can be perceived as a function approximator $D:F \rightarrow [0,1]c$, where F is the feature space where the object descriptions live, and c is the number of classes. While tuning such a function approximator outside the classification scenario would be very difficult, fuzzy classifiers may provide a solution that is both intuitive and useful (Kuncheva, 2000 and Mamdani, 1977).

b. Interpretability. Automatic classification in most challenging applications such as agricultural problems has been sidelined mostly due to the black box philosophy underpinning classical pattern recognition. Fuzzy classifiers are often designed to be transparent, i.e., steps and logic

statements leading to the class prediction are traceable and comprehensible (Kuncheva, 2003).

c. Limited data, available expertise. Examples include predicting and classification of rare diseases, oil depositions, terrorist activities, natural disasters. Fuzzy classifiers can be built using expert opinion, data or both.

2.1 Fuzzy rule-based classifiers

The simplest fuzzy rule-based classifier is a fuzzy if-then system, similar to that used in fuzzy control. Consider a 2D example with 3 classes. A fuzzy classifier can be constructed by specifying classification rules, e.g.

IF X1 is medium and X2 is small Then Class is 1

IF X1 is Medium and X2 is large Then Class is 2

IF X1 is large and X2 is small Then Class is 2

IF X1 is large and X2 is Large Then Class is 2

IF X1 is Large and X2 is small Then class is 3

If X1 is small and X2 is large Then Class is 3

The two features x1 and x2 are numerical but the rules use linguistic values. If there are M possible linguistic values for each feature, and n features in the problem, the number of possible different if-then rules of this conjunction type (AND) is Mn. If the fuzzy classifier comprises of all such rules, then it turns into a simple look-up table. Unlike look-up tables, however, fuzzy classifiers can provide outputs for combinations of linguistic values that are not included as one of the rules. Each linguistic value is represented by a membership function.

2.2 Methodology

The methodology of our work is geared toward specifying fuzzy rules utilizing fuzzy set theory application. We utilize several symptoms (S) of bacterial wilt (yellowish leaves, permanent wilted leaves, permanent upright leaves, brownish vascular tissues, dark brownish cortex and thin thread of ooze infected structure). Each of these symptoms fall into a rule (R1 - R6) and Label (High, moderate and low). The fuzzy rules Specifies

a. IF a plant exhibit S < 2 THEN Not Bacterial Wilt Recognized

b. IF a plant exhibits 2 $\leqslant$ S $\leqslant$ 4 THEN Moderately Bacterial Wilt Recognized

c. If a Plant exhibits S $\geqslant$ 5 THEN Bacterial Wilt Recognized

In set theory, the union (denoted by $\cup$) of a collection of sets is the set of all distinct elements in the collection. It is one of the fundamental operations through which sets can be combined and related to each other. The initial $\cup$ is initialized as R $\cup$ $\emptyset$ = R, for the set R. Therefore the fuzzy set rules are thus:

R0: R $\cup$ $\emptyset$

R1: {$\emptyset$ $\cup$ yellowish leaves} = Not Bacterial Wilt Recognized

R2: {Ø ∪ yellowish leaves} ∪ permanent wilted = Not Bacterial Wilt Recognized

R3: {Ø ∪ yellowish leaves ∪ permanent wilted} ∪ permanent upright leaves = Moderately Bacterial Wilt Recognized.

R4: {Ø ∪ yellowish leaves ∪ permanent wilted ∪ permanent upright} ∪ brownish vascular tissues = Moderately Bacterial Wilt Recognized.

R5: {Ø ∪ yellowish leaves ∪ permanent wilted ∪ permanent upright ∪ brownish vascular tissues} ∪ dark brownish cortex = Bacterial Wilt Recognized.

R6: {Ø ∪ yellowish leaves ∪ permanent wilted ∪ permanent upright ∪ brownish vascular tissues} ∪ dark brownish cortex} ∪ thin thread of ooze infected structure = Bacterial Wilt Recognized.

3 Results

The dataset stipulated on table 3.1 was derive from a research survey utilizing questionnaires as the research tools which was further analyzed utilizing line graph.

Table 3.1: Dataset Showing the Degree of Membership of Bacterial Wilt

PARAMETERS OR FUZZY SETS	CODES	DEGREE OF INTENSITY OF BACTERIAL WILT		
		Cluster 1 (C_1)	Cluster 2 (C_2)	Cluster 3 (C_3)
Yellowish Leaves	P01	0.50	0.00	0.50
Permanent Wilted Leaves	P02	0.20	0.50	0.60
Permanent Upright Leaves	P03	0.00	0.50	0.50
Brownish Vascular Tissues	P04	0.20	0.10	0.70
Dark Brownish Cortex	P05	0.30	0.60	0.10
Thin Thread Of Ooze Infected Structure	P06	0.05	0.05	0.90
RESULTS		**NOT BACTERIAL WILT RECOGNIZED**	**MODERATELY BACTERIAL WILT RECOGNIZED**	**BACTERIAL WILT RECOGNIZED**

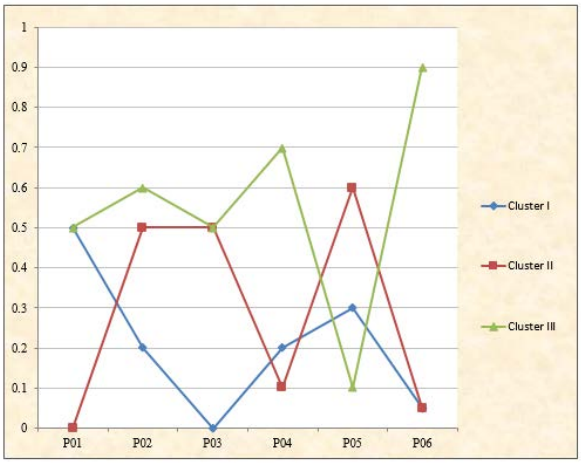

Figure 3.1: Graphical representation of Membership function for Bacterial Wilt

The graphical representation in Figure 3.1, is a representation of Table 3.1 and clearly show one criterion with high degree membership function of "Not Bacterial Wilt Recognized" in cluster 1, three criteria's with degree membership function of Moderately Bacterial Wilt Recognized" in cluster 2 and five criteria's with degree membership function of "Bacterial Wilt Recognized" in Cluster 3.

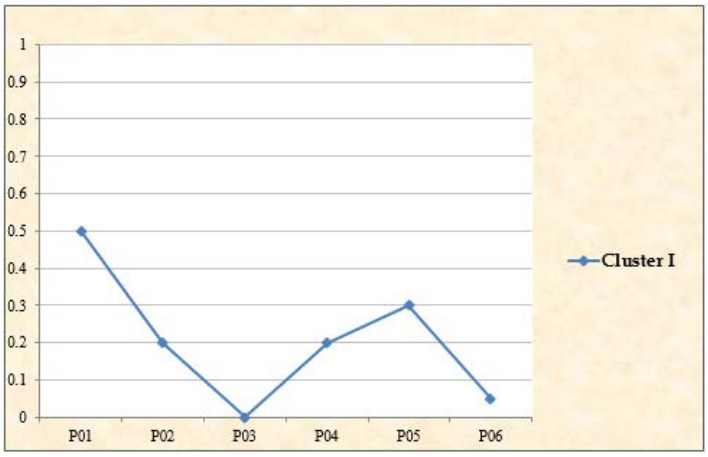

Figure 3.2: Graphical representation highlighting the degree of membership function for Cluster I of Bacterial Wilt

Figure 3.2 clearly shows one criterion with high degree of membership function in P01, and five criteria with Low degree of membership function in P02- P06.

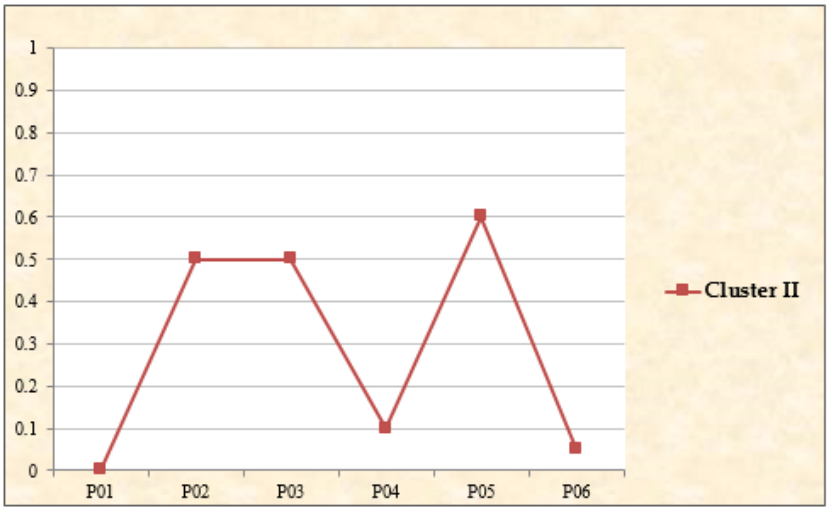

Figure 3.3: Graphical representation highlighting the degree of membership function for cluster II of Bacterial Wilt

Figure 3.3 clearly shows three criteria with high degree of membership function in P02, P03 and P05, and three criteria with low degree of membership function in P01, P02 and P06.

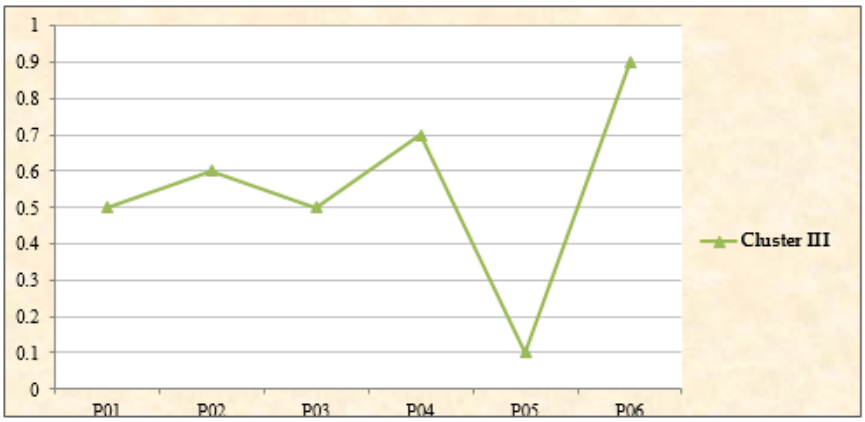

Figure 3.4: Graphical representation highlighting the degree of membership function for cluster III of Bacterial Wilt

Figure 3.4 clearly shows four criteria with high degree of membership function in P01- P04, and P06 and one criterion with low degree of membership function in P05.

4 Discussion

The main focus of our approach is geared toward recognizing bacterial wilt utilizing the rich facilities of fuzzy set theory application which is more pivotal in nature, flexible and robust. Unlike previous approaches which are times consuming and quite expensive because of repeated unnecessary test, this is just a simple based approach with interaction in merging plant symptoms exhibited.

5 Conclusion

Fuzzy logic with the aid of fuzzy-rules has been applied objectively to the recognition of bacterial wilt utilizing the symptoms sponsored and exhibited by each plant and the occurrence level at the point of exhibition. This approach has help us to objectively sub-divide plant symptoms occurrence into varied classes which is more precisely than the previous approaches.

REFERENCES

[1] Angelov P., Zhou X. (2008), Evolving Fuzzy-Rule-based Classifiers from Data Streams, IEEE Transactions on Fuzzy Systems, ISSN 1063-6706, special issue on Evolving Fuzzy Systems, December 2008, vol. 16, No6, Pp.1462-1475.

[2] Babuska R. (1998), Fuzzy Modeling for Control, Kluwer Academic Publishers, Boston, USA,

[3] Cordon O., Jesus M. J., Herrera F. (1999), A proposal on reasoning methods in fuzzy rule-based classification systems, International Journal of Approximate Reasoning, Vol. 20 (1), Pp.22-45.

[4] Gary W. M. (2014), "Bacterial Wilt -Ralstonia Solanacearum" retrieved from http://extension.psu.edu/pests/plant-diseases/all-fact-sheets/ralstonia

[5] Ishibuchi H., Nozaki K., Yamamoto N., Tanaka H. (1995), Selecting fuzzy if-then rules for classification problems using genetic algorithms, IEEE Trans. on Fuzzy Systems, 3(3), 1995, pp.260-270.

[6] Jones, R. K. (1993), Southern bacterial wilt, In Geranums IV, Geneva, IL: Ball Publishing.

[7] Kim, S. H., Olson, T. N., Schaad, N.W., and Moorman, G. W. (2003), Ralstonia solanacearum race 3, biovar 2, the causal agent of brown rot of potato, identified in geraniums in Pennsylvania, Delaware, and Connecticut. Plant Disease 87:450.

[8] Kuncheva L.I. (2000), Fuzzy Classifier Design, Springer-Verlag, Heidelberg

[9] Kuncheva L.I. (2003) "Fuzzy" vs "Non-fuzzy" in combining classifiers designed by boosting, IEEE Transactions on Fuzzy Systems, Vol.11 (6), 2003, Pp. 729-741.

[10] Lucas, G. B. (1975), Diseases of tobacco. Third ed. Raleigh, NC: Biological Consulting Associates.

[11] Mamdani E. H. (1977), Application of fuzzy logic to approximate reasoning using linguistic synthesis, IEEE Trans. Computers Vol. 26(12), 1977, Pp. 1182-1191.

[12] Nauck D., Klawonn F. and Kruse R. (1997), Foundations on Neuro-Fuzzy Systems, Wiley, Chichester

[13] Roubos J., Setnes M., Abony I J. (2003), Learning fuzzy classification rules from Data, Journal of Information Sciences, Vol. 150, Pp.77-93

[14] Takagi T. and M. Sugeno (1885), Fuzzy Identification of systems and its application to modeling and control, IEEE Trans. on Syst., Man & Cybernetics, 15, 1985, Pp. 116-132

[15] Yager R.R. and Kacprzyk J, (1997), "The Ordered Weighted Averaging operators". Theory and Applications, Kluwer Academic Publishers, USA,

SOCIETY FOR SCIENCE AND EDUCATION UNITED KINGDOM

JBEMi JOURNAL OF BIOMEDICAL ENGINEERING AND MEDICAL IMAGING

ISSN: 2055-1266
VOLUME 1, ISSUE 6

Neuro-Fuzzy Supervised Training Algorithm for Varied Chicken Disease Recognition

[1]Imianvan A.A. and [2]Obi J.C.
Department of Computer Science, University of Benin, Benin City. Nigeria
[1]tonyvanni@yahoo.com; [2]tripplejo2k2@yahoo.com

ABSTRACT

Poultry farming is an integral part of human existence. It link or interlink most, if not all of human endeavors which provides food in terms of meat and other proteins ingredients for human consumption and existence. Diseases on the other hand, are usually a resultant of human interaction with the ecosystem which has affected poultry farming for centuries. Most of the approaches applied in chicken disease recognition is subjective (based on the experiences, skills, exposure and talents of a personnel) in nature at best. Fuzzy Supervised Neural Network Training Algorithm has been designed and implemented with Matrix Laboratory (MATLAB) and Hypertext Pre-processor as the simulation tools and language respectively. This paper demonstrates the practical application of algorithm techniques in medical the agricultural sector with the aim of distinctive recognition of four classes of chicken disease.

Keywords: chicken disease, Fuzzy set, Fuzzy Logic, Algorithm, Supervised-Neural-Network

1 Introduction

Poultry farming is the raising of domesticated birds such as chickens, turkeys, ducks, and geese, for the purpose of farming meat or eggs for food. Poultry are farmed in great numbers with chickens being the most numerous. More than 50 billion chickens are raised annually as a source of food, for both their meat and their eggs (Sherwin et al., 2010). Chickens raised for eggs are usually called layers while chickens raised for meat are often called broilers (Grandin and Johnson, 2005).

Commercial hens usually begin laying eggs at 16–20 weeks of age, although production gradually declines soon after from approximately 25 weeks of age (Singer, 2006). This means that in many countries, by approximately 72 weeks of age, flocks are considered economically unviable and are slaughtered after approximately 12 months of egg production (Hernandez, 2005) although chickens will naturally live for 6 or more years. In some countries, hens are force moulted to re-invigorate egg-laying. Environmental conditions are often automatically controlled in egg-laying systems (Jonathan, 2011). For example, the duration of the light phase is initially increased to prompt the beginning of egg-laying at 16–20 weeks of age and then mimics summer day-length which stimulates the hens to continue lying all year round; normally, egg production occurs only in the warmer months. Some commercial breeds of hen can produce over 300 eggs a year (Jonathan, 2011). Critics argue that year-round egg production stresses the birds more than normal seasonal production.

DOI: 10.14738/jbemi.16.762
Publication Date: 2st January 2015
URL: http://dx.doi.org/10.14738/jbemi.16.762

There are two main poultry rearing approach, these includes:

a. Free-range poultry farming allows chickens to roam freely for a period of the day, although they are usually confined in sheds at night to protect them from predators or kept indoors if the weather is particularly bad.

Figure 1: Commercial free range hens

The benefits of free-range poultry farming for laying hens include opportunities for natural behaviours such as pecking, scratching, foraging and exercise outdoors (Jonathan, 2011).

Both intensive and free-range farming have animal welfare concerns. Cannibalism, feather pecking and vent pecking can be common with some farmers using beak trimming as a preventative measure, although reducing stocking rates would eliminate these problems. Diseases can be common and the animals are vulnerable to predators (Sherwin et al., 2010).

b. The majority of hens in many countries are reared in battery cages. These are small cages, usually made of metal in modern systems, housing 3 to 8 hens. The walls are made of either solid metal or mesh, and the floor is sloped wire mesh to allow the faces to drop through and eggs to roll onto an egg-collecting conveyor belt. Water is usually provided by overhead nipple systems, and food in a trough along the front of the cage replenished at regular intervals by a mechanical chain (Adler and Lawler, 2012).

Figure 2: Hens in a battery cage system

Majority of diseases affecting poultry bird are usually tied to the respiratory organ of the system which usually interlink with other system such as air sac of the body. The respiratory system are usually are of particular note to poultry bird because of the easy of disease flow and spread (Local Harvest, 2010).

The focal point of this research is geared toward recognizing four common poultry disease utilizing a Neuro-Fuzzy (Neural Network and Fuzzy Logic) Algorithm approach.

2 Material and Method

Four common chicken diseases are: (Local Harvest, 2010)

a. **Infectious Bronchitis**: Infectious Bronchitis is a diseases respiratory based in backyard flock chickens that is relatively common. This condition is also known as "Bronchitis" and a "Cold". This disease is specific to chickens in particular when it comes to types of poultry. The infection may be mild to severe, depending on several circumstances such as the strength of the immunity of the bird, and other conditions present in the environment in which the chicken is located. Chicken diseases symptoms that are present when it comes to this particular illness include, but are not limited to:

P1: Lack of regular food consumption

P2: Liquid discharge in eyes and nostrils

P3: Breathing complications with gasping

P4: Distinguishable chirping sounds

P5: Reduced dramatically egg production

b. **Avian Influenza**: Many chicken owners have discovered that the chickens in their flocks come down with a condition which is called "Avian Influenza". This is also known as the "Fowl Plague", and the "Flu". While any type of bird may acquire this illness, chicken owners should be concerned because of the fact that it can spread rapidly through flocks. There are many ways that this condition can be transmitted from one chicken to another, making it a large concern when it comes to diseases respiratory in home flocks. These methods include contamination by shoes that can carry it from one location to another, insects, rodents, and even equipment used in chicken coops and the basic care of chickens. Chicken diseases symptoms may include any or all of the following:

P6: Respiratory function distress

P7: Rapid eating habits change

P8: Mild-severe diarrhea

P9: Decrease in egg production rates

P10: Reddish or whitish spot on the legs of the chicken affected

P11: Irritated legs, and wings

c. **Mycoplasma Galliseptiu**: Mycoplasma Gallisepticum or "Chronic Respiratory Disease" is a disease in respiratory system that many chickens may be affected by. Many may also refer to

this illness as "Mycoplasmosis" or "Infectious Sinusitis". While poultry such as turkeys and ducks may be affected by this condition, backyard flock chickens are commonly affected as well. Chicken diseases symptoms present with these diseases in respiratory system include:

P12: Swollen sinuses

P13: An obvious sneeze may become apparent

P14: Discharge may be emitted through the nasal cavity

P15: A foamy based discharge may be evident in the eyes

P16: Unusual sounds emitted when taking breaths

d. **Fowl Pox**: Fowl Pox is another common chicken disease found in backyard flocks. This is known by many names, such as "Chicken Pox" (Not the same as the human version), "Bird Pox", and "Avian Diphtheria". When poultry suffers from these diseases respiratory, there are many chicken diseases symptoms present, such as:

P17: Lesions that reflect that of "warts" often appear on the areas of the body where there are no feathers

P18: Egg production rate is typically hindered

P19: The skin may appear raw, and this may be accompanied by bleeding

P20: Noticeable distress in respiratory function

P21: Congestion in the respiratory system may be experienced

The theory of fuzzy logic provides a mathematical strength to capture the uncertainties associated with human cognitive processes, such as thinking and reasoning. In standard set theory, an object does or does not belong to a set. There is no middle ground. In such bivalent systems, an object cannot belong to both its set and its compliment set or to neither of them. This principle preserves the structure of the logic and avoids the contradiction of object that both is and is not a thing at the same time (Zadeh, 1965). However, fuzzy logic is highly abstract and employs heuristic (experiment) requiring human experts to discover rules about data relationship (Angel and Rocio, 2011).

Fuzzy classification assumes the boundary between two neighboring classes as a continuous, overlapping area within which an object has partial membership in each class (Kuang et al., 2011). Fuzzy logic highlights the significant of most applications in which categories have fuzzy boundaries, but also provides a simple representation of the potentially complex partition of the feature space. (Sun and Jang, 1993 and Ahmad, 2011) Conventional approaches of pattern classification involve clustering training samples and associating clusters to given categories. The complexity and limitations of previous mechanisms are largely due to the lack of an effective way of defining the boundaries among clusters. This problem becomes more intractable when the number of features used for classification increases (Christos and Dimitros, 2008).

Artificial Neural Networks (ANNs) constitute a class of flexible nonlinear models designed to mimic biological neural systems. An ANN is a mathematical model or computational model based on biological

neural networks (Gutiérrez, 2011), as an interconnected group of artificial neurons, which carries out computation using a connectionist approach. Typically, a biological neural system consists of several layers, each with a large number of neural units (neurons) that can process the information in a parallel manner. The models with these features are known as ANN models (Robert, 2000). ANNs have been widely applied to solve many difficult problems in different areas, including pattern recognition (matching), signal processing, language learning, electronic medical record processing, tele-diagnosis and computer networking (Robert, 2000). Neural network utilize dataset. The data set is divided into three distinct sets: training, testing and validation sets. The training set is the largest set and is used by neural network to learn patterns present in the data. The testing set is used to evaluate the generalization ability of a supposedly trained network. A final check on the performance of the trained network is made using validation set. Learning methods in neural networks can be broadly classified into three basic types Supervised, unsupervised and reinforced learning (Diogo et al. 2008).

Supervised learning is the machine learning task of inferring a function from supervised training data. The training data consist of a set of training examples. In supervised learning, each example is a pair consisting of an input object (typically a vector) and a desired output value (also called the supervisory signal). A supervised learning algorithm analyzes the training data and produces an inferred function, which is called a classifier (if the output is discrete) or a regression function (if the output is continuous).

Unsupervised learning studies how systems can learn to represent particular input patterns in a way that reflects the statistical structure of the overall collection of input patterns. By contrast with Supervised Learning or Reinforcement Learning, there are no explicit target outputs or environmental evaluations associated with each input; rather the unsupervised learner brings to bear prior biases as to what aspects of the structure of the input should be captured in the output. Unsupervised learning is important since it is likely to be much more common in the brain than supervised learning (Benedetti et al., 2005).

Reinforcement learning, one of the most active research areas in artificial intelligence, is a computational approach to learning whereby an agent tries to maximize the total amount of reward it receives when interacting with a complex, uncertain environment. Reinforcement learning provides a clear and simple account of the key ideas and algorithms. Their target ranges from the history of the field's intellectual foundations to the most recent developments and applications. The only necessary mathematical background is familiarity with elementary concepts of probability (Richard and Andrew, 2011).

The four most widely used neural networks are the feed-forward networks and recurrent or interactive (feedback) networks, kohonen's self-organizing network, Adaptive resonance Theory (ART) and Counter propagation network are others (Chakraborty, 2010).

Feed-forward ANNs allow signals to travel one way only; from input to output. There is no feedback (loops) i.e. the output of any layer does not affect that same layer. They are extensively used in pattern recognition (Chakraborty, 2010).

This multi-layered structure of a feed-forward network is designed to function as a biological neural system. The input units are the neurons that receive the information (stimuli) from the outside environment and pass them to the neurons in a middle layer (i.e., hidden units). These neurons then

transform the input signals to generate neural signals and forward them to the neurons in the output layer. The output neurons in turn generate signals that determine the action to be taken. It is important to note that all information from the units in one layer is processed simultaneously, rather than sequentially, by the units in an "upper" layer (kuan and white, 1994).

Feedback Network or Recurrent Neural Networks: Feedback networks can have signals travelling in both directions by introducing loops in the network. Feedback networks are dynamic; their 'state' is changing continuously until they reach an equilibrium point. They remain at the equilibrium point until the input changes and a new equilibrium needs to be found (Chakraborty, 2010).

Kohonen's Self-Organizing Network is a two-layer, feed-forward network (Beale and Jackson, 1990 and Dayhoff, 1990).The first is an input layer and the second is a grid or map arranged in a one or two-dimensional array. The second layer is known as a competitive layer. Incoming patterns are classified by the nodes that they activate in the competitive layer. Similarities among patterns are mapped into closeness relationships on the competitive layer. After training, the pattern relationships and groupings are observed from this layer.

Adaptive Resonance Theory (ART) is an unsupervised, competitive learning algorithm (Beale and Jackson, 1990). It is a two-layer network arranged in feedback and feed-forward connection. The layers have different functions, unlike the Multilayer or Kohonen networks. The first layer can be either an input or a comparison layer and the second layer can be either an output or a recognition layer. Both are interchangeable during training.

2.1 Method: The Proposed Neuro-Fuzzy Supervised Training Algorithm for Varied Chicken Disease Recognition

The proposed Algorithm imbibes artificial intelligence techniques in tying the symptoms of chicken disease to the differential recognition of four classes thereby establishing a conclusive boundary. Unlike the current approaches, in which success or failure are based on the wills and experiences of relevant personnel designing and administrating the approach in other to elicit relevant recognition points. The forecasted algorithm is artificial intelligence based; therefore success and failure are not dependent on human intuitions, but success is closely linked to the tuned-up components of the systematic implemented approach. The Algorithm is depicted on Figure 1

INPUT:

Types of Chicken Disease (Infectious Bronchitis, Avian Influenza, Mycoplasma Galliseptiu, and Fowl Pox,)

No. of Symptoms (P1, P2, P3…, Pn) = 20
P; Fuzzy parameters (Symptoms Codes)

Degree of membership function

≥ 0.50 = High degree membership function (serious)
< 0.50 = Low degree Membership Function (minor)

Fuzzy predefined Rules

More than five symptoms = Diagnose with a class of Chicken disease
Exactly four symptoms = Might be diagnose with a Chicken disease
Three symptoms and below = Not diagnose with a Chicken disease

// **INITIALIZATION**

1. Randomly pick a Chicken *K;*
2. Save identification (recognition) Result in *Knot;*

// Loop till terminal point

3. For P = 1 to n do;

// **INFECTIOUS BRONCHITIS**

4. Recognize for **Infectious Bronchitis**
5. If symptoms are ***P1-P5***, symptoms membership are ***serious*****,** and symptoms ≥ ***five*** THEN infectious bronchitis;
6. Else if
7. Might be **Infectious Bronchitis**; (symptoms = ***four***);
8. Else
9. Not **Infectious Bronchitis** (symptoms ***≤ three***);

// **AVIAN INFLUENZA**

10. Recognize for **Avian Influenza**;
11. If symptoms are ***P6-P11***, symptoms membership are ***serious*****,** and symptoms ≥ ***five*** THEN **Avian Influenza**;
12. Else if
13. Might be **Avian Influenza** (symptoms = ***four***);
14. Else
15. Not **Avian Influenza** (symptoms ***≤ three***);

//**MYCOPLASMA GALLISEPTIU**

16. recognize for **Mycoplasma Galliseptiu**;
17. If symptoms are ***P12-P16,*** symptoms membership are ***serious*****,** and symptoms ≥ ***five*** THEN **Mycoplasma Galliseptiu**;
18. Else if
19. Might be **Mycoplasma Galliseptiu** (symptoms = ***four***);
20. Else
21. Not **Mycoplasma Galliseptiu** (symptoms ***≤ three***);

//**Fowl Pox**

22. recognize for **Fowl Pox**;
23. If symptoms are **P17- P21**, symptoms membership are serious, and symptoms ≥ five THEN **Fowl Pox**;
24. Else if
25. Might be **Fowl Pox** (symptoms = four);
26. Else
27. Not **Fowl Pox** (symptoms ≤ three);

//Save results in *Knot;*

28. Return chicken disease result for chicken K

Figure 1: The Proposed Neuro-Fuzzy Supervised Training Algorithm for Varied Chicken Disease Recognition

3 Implementation and Discussion

The implementation of our result was dual fold; the neural training dataset was handled conveniently utilizing Matrix Laboratory (MATLAB) which serves as our simulation tool in achieving the our results because of its interactive environment for algorithm development, data visualization, data analysis, and numerical approach which was relevant to our numerical dataset which was more appropriate than with

spread-sheets or traditional programming languages, such as C/C++ or Java. MATLAB was essential in validating some of the if-then rules concept with the training algorithm. The design alternatives was distributed and visualized in various concept utilizing MATLAB tools. The debugging tools in MATLAB were useful in identifying underlying errors and eliminating them. After pruning the dataset utilizing MATLAB the algorithm was fully implemented utilizing Hypertext Preprocessor (PHP), which served as the language of implementation. PHP provide the languages for writing the dynamic web-pages which enable any veterinary personal to access the system online retrieved relevant information in determining the relevant diseases.

4 Discussion

The implemented algorithm provides an interactive base in determining varied chicken disease objectively as opposed to the subjective approach which is achievable utilizing the subjective approach. The result was satisfactory having been able to distinctively recognize several chicken disease and subsequently classified into varied classes.

5 Conclusions

This paper has demonstrated the practical application of neuro- fuzzy supervised training algorithm in the agricultural sector by providing a means of recognizing varied chicken disease.

REFERENCES

[1] Adler J.; Lawler A. (2012), How the Chicken Conquered the World, Smithsonian, Retrieved May 27, 2012.

[2] Ahmad H. (2011), Fuzzy approach to Likert Spectrum in Classified levels in surveying Researches retrieved http://www.tjmcs.com.

[3] Angel C. and Rocio R. (2011), Documentation management with Ant colony Optimization Meta-heuristic: A Fuzzy Text Clustering Approach Using Pheromone trails, retrieved from soft computing in Industrial applications, Advances in intelligent and soft Computing, vol. 96, 2011, 261-70, DOI: 10.1007/978-3-642-20505-1_23

[4] Benedetti S., Saverio M., Anna G. S. and Gian L.M. (2005), Electronic nose and neural network use for the classification of honeypot, retrieved from citeseerx.ist.psu. Edu/viewdoc /download?doi=10.1.1.128.pdf

[5] Beale R. and Jackson I. (1990), Neural Computing: An Introduction, dl.acm.org/citation.cfm?id=121342.

[6] Chakraborty R.C. (2010), Soft computing-Introduction: Soft-computing Lecture 1-6, notes, retrieved from http://myreaders.inro

[7] Christos S. and Dimitros S. (2008) Neural Network, retrieved from http://www.docstoc.com/docs/15050/neural-networks.

[8] Dayhoff, J.E. (1990), Neural Network Architecture: An Introduction, retrieved from https://catalyst.library.jhu.edu/?q=%22Dayhoff%2C+Judith.

[9] Diogo F. P., Flávio R.S. O. and Fernando B. L. N (2008), Multi-objective abilities in the Hybrid Intelligent Suite for decision support, retrieved from http://ieeexplore. ieee.org/xpl/freeabs_all.

[10] Grandin T.; Johnson, C. (2005), Animals in Translation, New York, NY: Scribner. Pp. 183, ISBN 0-7432-4769-8.

[11] Gutiérrez P.A. (2011), Hybrid Artificial Neural Networks: Models, retrieved online from http:// dl.acm.org/citation.cfm?id=20233.

[12] Hernandez N., (2005), Advocates Challenge Humane-Care Label on Md. Eggs. Washington Post, Retrieved 2009-07-30.

[13] Jonathan S. (2011). Delaware business: Chicken companies feeling pinch as corn prices soar, News Journal (Gannett), Delaware-Online. OCLC 38962480. Retrieved 10 April 2011.

[14] Kuan C. M. and White H. (1994), Artificial neural networks: An econometric perspective, Econometric Reviews, Vol.13, Pp.1-91 and Pp.139-143.

[15] Kuang Y. H.; Ting-H. C. and Ting-Cheng Chang (2011), Determination of the threshold value β of variable precision rough set by fuzzy algorithms, retrieved from http://www.sciencedirect.com/science/article/pii/S0888613X11000831.

[16] LocalHarvest, (2010), Common Chicken Diseases and Symptoms in Backyard Flocks http: //www.localharvest.org/blog/26992/entry/common_chicken_diseases_and_symptoms.,

[17] Richard S. S. and Andrew G. B. (2011), Reinforcement learning: an Introduction, retrieved from http://books.google.com/books/about/Reinforcement_l.

[18] Robert F. (2000), Introduction to Neuro-Fuzzy Systems: Advances in Soft Computing Series, Springer-Verlag, Berlin/Heidelberg, Germany.

[19] Sherwin, C.M., Richards G.J and Nicol C.J. (2010), A comparison of the welfare of layer hens in four housing systems in the UK. British Poultry Science, 51(4): 488-499.

[20] Singer P. (2006), In Defence of Animals, Wiley-Blackwell, Pp. 176, ISBN 1-4051-1941-1.

[21] Sun C.T. and Jang J.S. (1993) A neuro-fuzzy classifier and its applications, in: Proc. IEEE Int. Conference on Neural Networks, San Francisco, pp.94–98.

[22] Zadeh L.A. (1965), Fuzzy sets, Journal of Information and Control", Vol.8, pp.338-353.

SOCIETY FOR SCIENCE AND EDUCATION UNITED KINGDOM

JBEMi JOURNAL OF BIOMEDICAL ENGINEERING AND MEDICAL IMAGING

ISSN: 2055-1266
VOLUME 1, ISSUE 6

A Help for Assisting People Based on a Depth Cameras System Dedicated to Elderly and Dependent People

[1,2]Asma Ben Hadj Mohamed, [1]Thierry Val, [1]Laurent Andrieux, and [2]Abdennaceur kachouri

[1]CNRS-IRIT, Toulouse 2 University, France

[2]Laboratory of Electronic and Technical Information, National School of Engineers of Sfax, Tunisia

asma.ben-hadj-mohamed@irit.fr; val@irit.fr; laurent.andrieux@univ-tlse2.fr

Abdennaceur.Kachouri@enis.rnu.tn

ABSTRACT

In this paper, we propose a help to a comfort system development based on Kinect sensor to assist people commanding their own house by using only their gestures. The system uses a multi-sensors to detect the person, recognize her gestures and communicate through an IP/KNX gateway to act on actuators related to the home. Thus, a simple gesture is able to turn on/off the lights, to switch on/off the TV, to move up or down the shutters etc. We performed a test bed within the smart home of our University Institute of Technology in Blagnac.

Keywords: home automation; Kinect; elderly control; sensor network; smart home; gesture recognition

1 Introduction

In recent years, the decline of mortality and fertility rates at the same time has made the life expectancy increased. Therefore, the proportion of the elderly population raised up remarkably all over the world especially in European Union and Canada (see Figure 1). The rate of elderly population is increasing and is estimated to reach almost 30 % of the population in Canada in 2060 [1].This aging has many impacts on the physical and cognitive health, the economy of the country and the health care spending [2][3][4]. This has engaged the researchers to study the phenomenon and to seek solutions to monitor, control and help to comfort for this category of people.

Home automation is a field of research that aims to keep the elderly or disabled healthy and sound in their own home and facilitate their daily tasks. With the emergence of technology in our daily lives, it's time to share it with these people for their own welfare. However, it's necessary to respond to their needs. The most important is to present a soft, simple, not expensive and especially not intrusive solution.

The classical idea of an accompanying nurse might interfere with patient privacy. However, using a sensor network to collect various data relating the state of the person, or supervising any change in her environment, represents a very advantageous solution for several reasons. On the economic front, monitoring an elderly or disabled person while keeping him in his natural environment would reduce the costs of assistance compared to specialized hospital staff, or to a nurse at home. A significant contribution concerns the psychological and social side of the dependent person, to whom this discreet

DOI: 10.14738/jbemi.16.782
Publication Date: 2st January 2015
URL: http://dx.doi.org/10.14738/jbemi.16.782

and imperceptible monitoring provides a sense of security, privacy respect and autonomy [5]. In this paper, we present a part of a generic work whose topic is the monitoring of elderly people living in a smart home. The overall objective is maintaining these persons at home and giving them the feeling of safety and comfort.

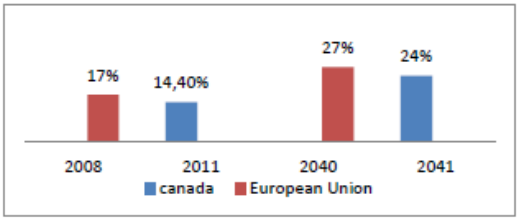

Figure 1: Percentage of people aged more than 65 in EU and Canada, and forecasts by 2040 [1][2]

2 The Existing Solutions

The technological revolution in electronics, computer science and wireless sensors networks, has enabled many changes in the medical field, which has greatly evolved over the last years. Indeed, the progress in biomedical instrumentation, implants, prosthetics, biomaterials and medical computing are impressive. Other branches of medicine in continuous progress are telemedicine and health services, such as home tele-monitoring, home automation, health care networks and management of medical tests multi-center. Thus, this positive evolution of medical technologies makes a big business for large companies.

Some solutions such as biometric sensors, who can be integrated on patient's body and control their medical states, are commonly used. In many cases, these devices must be closed or fixed on the body y using belts, watches or patches [6].They can disturb patients and limit their mobility as well as their comfort [7]. Other commercial solutions exist and do not impede the mobility of people and their liberty. They are efficient to track the movements of the person and they can detect the risk of incidents such as a fall. We mention the LysBox device as a good example. It is a small box which can be fixed on the walls in the rooms of the house and monitor the patient [8]. However, it needs a learning period of a few days or weeks to track and learn the person's habits via an internet connection. Some research projects facilitate domestic works by controlling elderly environment through computer systems and touch interfaces employed everywhere in the house. We cite the most remarkable in the field such DOMUS project [9]. It consists of a complete hardware and software system (servers, software application, computer interfaces, Internet, mobile nodes deployed in the patient's environment) to gather information from temperature, pressure, humidity sensors, and communicate instructions/actions to the home devices to be controlled via internal communication network allowing the exchange of messages between the control system and the devices. Thus, it controls automatically the state of the environment. However, the installation of such a system requires a large number of sensors and devices, with a consequent budget. Another interesting research project is called HOMECARE [10] [11]. It provides indoor monitoring for elderly persons with cognitive disease (such as Alzheimer) or loss of independence. It fits in simple devices (patch and shoe sole) to communicate patient status. Clinical studies and tests have shown that the system is accepted by the patients in 80% of cases, and reliable in case of home treatment (correct fall detection for 98% of cases). However, this

system is less trusted when it is applied to a large mass of people (like in hospitals or nursing homes), since the results demonstrate a false fall down average detection every 4 days for one person. Besides, developed devices are attached to the patient's body even if it's in an indiscreet position, which can impede patients.

We can also quote The Guardian Angel project [12]. It aims to produce miniature sensors, integrated on any media type, and capable of self-sustaining energy from the surrounding. The monitoring of various parameters related to health and environment is at the fore front for applications. The project is being developed in partnership with many strong companies and research laboratories [13].

3 Our Contribution for Help to Comfort

Starting on already made project ideas, we thought about a comfort support system for this type of person, easy to install and use, cheaper and able to control the home environment easily. People with reduced mobility can thus perform some actions only with gestures, without having to move or make the slightest effort. We also thought to respect the privacy and the feeling of comfort by not attaching sensors to the body. So, our proposition consists in a system development based on depth camera network. Our solution is able to detect patients at home and recognize their gestures in aim to react to their needs (open or close a door, turn on or turn off the lights, etc.). Thus, the general idea is to design a smart environment controlled by people gestures without using remote control, joysticks, push buttons, keyboards or even touch interfaces. The peculiarity of this application also lies in the use of a sensor initially designed for video game.

3.1 Improve Kinect sensor features

The choice of Kinect video sensor was made for its features. Initially dedicated to video games systems, it is now used in many applications such as robotic, industry, video games etc[14]. Indeed, it includes a depth camera which is able to monitor people, by respecting theirs identity and privacy, since 3D images hide body details. In addition, the libraries supplied with the software kit of the sensor allow a wide use of depth, color and skeleton data stream. Until today, three versions of the Kinect hardware have been developed: the Kinect for XBOX, the Kinect for Windows and the Kinect for windows 2.0. Tables 1 details characteristics of each version. We used Kinect for XBOX for our application.

Table 1: KINECT sensors characteristics

Property	Kinect for XBOX	Kinect for Windows 1	Kinect for Window 2.0
Field of View	57° H, 43° V	57° H, 43° V	70°H, 60° V
Data interface	USB 2.0	USB 2.0	USB 3.0
Depth range	1.8m-4m	0.4m-4.0m	0.4m-4.5m
Color stream	640x480@30FPS	640x480@30FPS	1920x1080@30FPS
Depth stream	320x240	320x240	512x424
Infrared stream	None	None	512x424
Audio stream	4 mic-array	4 mic-array	4 mic-array
Tits motor	Yes	Yes	No
Skeleton joints	20	20	26
Supported OS	Win 7	Win 7, Win 8	Win 8
Near mode	No	Yes	Yes
Full skeletons trucked	2	2	6
Price	$99	$223	$399

The kinect sensor operates as follows: first, Kinect emits IR lights. Combinated with the "time to flight" values, reflections of the laser beam are computed using a highly parallel System on Chip called “PS1080”. The sensor receives a coded infrared light (IR) as input, and produces a colorized picture, an audio stream and a depth image. All of them are synchronized with a VGA format. The most interesting element of this specific sensor is the depth camera that captures the3D scene. In other words, the pixels of the depth image represent the coordinates (x, y, z) of the scene objects. This depth image is insensitive to variations in brightness and contrast levels. Therefore, it is able to work in a dark room thanks to active infrared lights. Thus, it is very useful for monitoring a person in a dark environment.

3.2 The smart home

This work focuses on the detection and recognition of gestures using depth sensor which provides depth images. The smart house is located within the University Institute of technology in Blagnac. A 3D view of this house is shown in Figure 2.

Figure 2: The Smart Home using Kinect sensors © IUT Blagnac [15]

4 Commanding the Smart Home with Gesture

4.1 Gesture recognition using Kinect sensor

The idea is to implement relatively simple gestures dedicated to these categories of people to make their tasks easier. We made a gesture recognition using hands position. In human body 20 joints are recognized using Kinect sensor [16]. If we compute the coordinates (x, y, z) of each joint in the space we can have an idea about the position of each part of the body referred to the head or spin joint. We have to process the depth and skeleton frame to search the body coordinates of the person, and recognize if hands are below or overhead/spin, or if the patient is showing the right or the left direction.

We have computed the coordinates (in meter) of the right hand in every case. Some of these recognized postures we made are implemented in a database and illustrated in Figure 3. These gestures will be useful, for example, to turn on/off lights in the living room. We have also implemented a focus gesture based on Z coordinates in the space. We choose a threshold distance, so if the patient is not moving in the scene, the program is in an idle mode. A push and pull gesture is detected when there is a 20 cm threshold on the Z axis of each hand. It is illustrated in Figure 4. This gesture will serve to open or close

the entry door. It is also possible to recognize a gesture as "Hello", or a "skip-like" gesture with hands, in the same way as a person can manipulate a tactile panel. Through these 4 examples, our system is able to interpret many gestures without making the slightest effort.

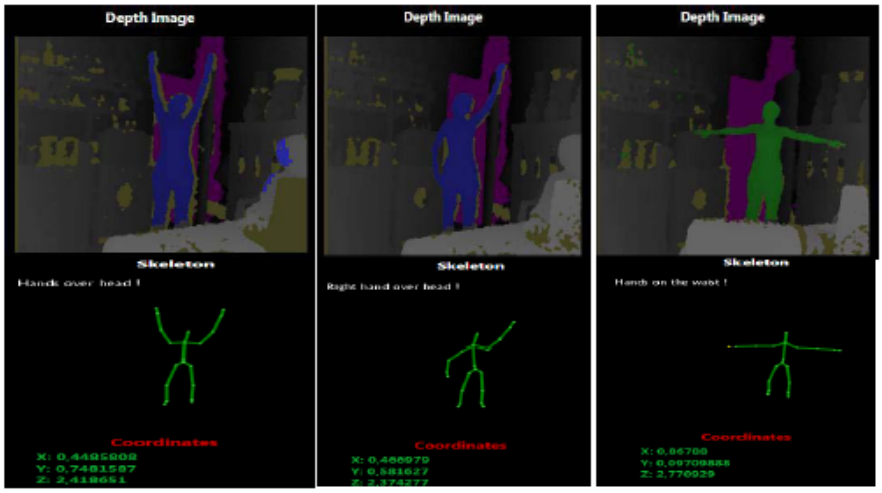

Figure 3: Recognition of 3 different gestures in depth and skeleton frames

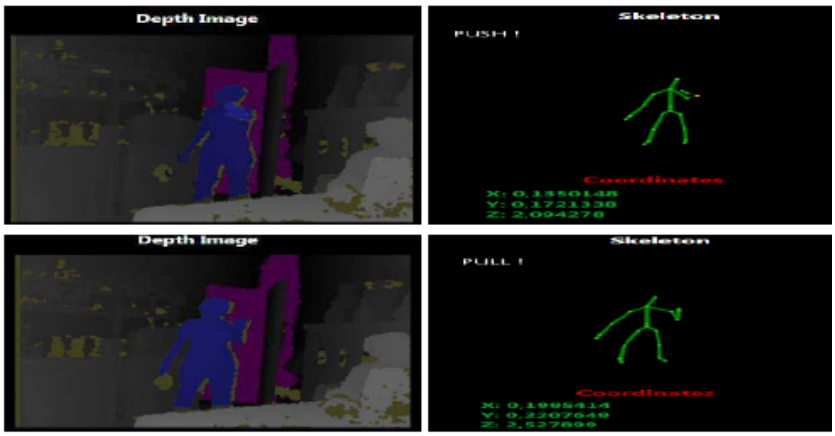

Figure 4: Recognition of push and pull gesture

If we want to recognize a large number of gestures useful in our application, two methods are existing: algorithmic or template based search. The main challenge is to choose the most appropriate method. Neural networks or Hidden Markov Model (HMM) are very sophisticated [9].

However, they require a training (also called learning) time on the wanted form before being saved [10]. This makes these types of algorithms less convenient for prototyping, in which, the user or developer wants to define its own recognizable and recordable form. In addition, this level of sophistication leads to a difficulty in both debugging and programming. However, other algorithms such as the one dollar ($1) [20] and N dollar ($N) recognizers [21], can be implemented in any environment, even in a context of fast prototyping [22].

4.2 Unistroke gesture recognition

Every gesture is defined by a set of points. These points are compared to another set of points previously stored. From this, it may be deduced that only the comparison between each one of these points is not sufficient to determine the best "candidate point" among sets of points. The templates to recognize gestures are the variations between two gestures made by the same person but at different speeds and / or different figure. They will not generate the same number of points and the comparison is not based only on this single criterion. Furthermore, we have to notice that other problems are occurring: orientation, scale gesture/figure and corners. The $1 recognizer algorithm [20] is insensitive to all these types of variations. The learning of a gesture is performed only one time, which means it only requires a single pass to create a template unlike Hidden Markov Models (HMM) and neural networks. It should also be noticed that the $ 1 recognizer considers only "Unistroked" movements, which means a single figure is formed by a continuous gesture, contrary to "Multistroke" movements. The one dollar Unistroke recognizer is defined as four steps. The first three steps are done to create templates for the first time in order to compare them in the immediate future.

- Resampling
- Rotation based on indicative angle
- Scaling and translation
- Get the best score

This score is calculated using the equation:

$$\text{Score} = 1 - \frac{d_i^*}{\frac{1}{2}\sqrt{(size^2+size^2)}} \quad (1)$$

Where

$$\frac{\sum_{k=1}^{N}\sqrt{(C_x[k]-T_x[k])^2+(C_y[k]-T_y[k])^2}}{N} = d_i \quad (2)$$

d_i: The minimum path distance between C and

d_i: The path distance

C: Candidate points

T_i: The points of each of the templates

Thus, it is possible to integrate another recognizer algorithm such as $1 or $N into our application. The diagram of the recognition scenario proposed is represented in Figure 5. If an action is detected, we focus on hands position to see if there is a specific gesture that allows to trigger a recognition. The push and pull gesture can be another event allowing to trigger another recognition. We mentioned that the implementation of the $1 algorithm will be done in the future work.

Figure 5: Diagram of gesture recognition using Kinect

At this stage, we used a toolbox included in the Kinect Software Development Kit. This toolbox uses a combination of Golden Section Search and one $1 method. Therefore, the implementation is able to recognize some other gestures like a circle (see Figure 6).

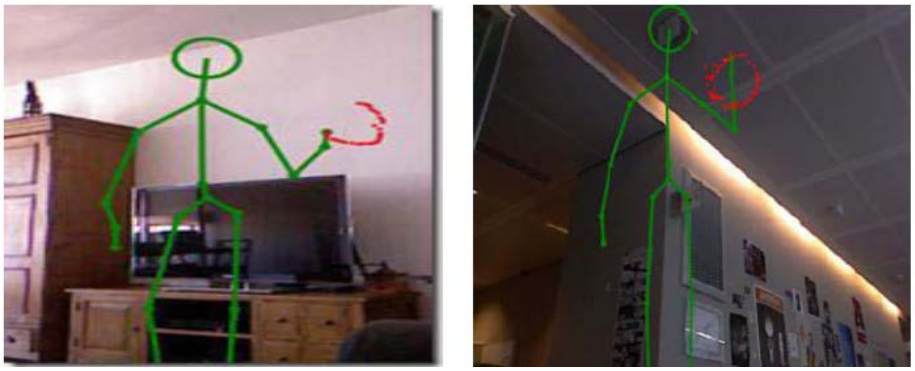

Figure 6: Examples of using Kinect toolbox to recognize a circle gesture [23].

In the next section, we present how we interface the kinect sensors to the actuators, by interconnecting the IP network with KNX bus. We detail how we turn on and off the lights and generate a voice message corresponding to the action.

5 Network communication

5.1 Setting up the Kinect network

Depending on the size of the house or the hospital, we may need a lot of Kinect sensors that will link to a network (wired Ethernet or wireless WiFi ...). In a parallel work, we have already tested a Kinect wireless sensor network using Mesh WIFI [25]. We have also discussed the use of a WIFI network with mesh topology. Indeed, we test the application of OLSR routing protocol [26] and 802.11s standard [27]. We

implemented 802.11s which enables network operation, and we checked its feasibility and validity by getting response time and quality of transmission between wireless nodes.

For each node, we have investigated the response time and the link quality. We also tried to transport Kinect data (depth images) through the network using USB over IP encapsulation [18].

Results show that it is difficult to broadcast data through the mesh network due to the high throughput required in the network which was about 180 MBits/s [25]. Therefore, we choose to communicate a simple sign. So, when an action is detected, we don't have to communicate all the frames through the network. A specific frame including a text or an alert will be sufficient. We tested our solution by sending an alert signal over the network.

In case of falling down or emergency situation, we send alert frames via the network to see if the patient is safe. Anyway, the transmission of a message within the network seems discreet and easy, and does not represent any kind of the patient spying in their own home. In the next section, we will represent the network architecture between the Kinects connected on IP (Ethernet, WiFi802.11s or a simple WiFi) and the smart home actuators connected on KNX bus.

5.2 Interconnection IP/KNX

KNX (KONNEX) or EIBUS (European Installation Bus) is an European standard bus and for building automation [24]. Unlike other automation protocols, it does not work in master/slave mode, but each node is independent of the others. It supports various communication mediums such as Ethernet, radio, and power-line communication. The advantage of using this KNX home automation network is its flexibility when changing the building topology without demolishing walls or installing new circuits and wiring. He brings over some comfort by simplifying everyday life. The system is also cost-effective and provides low-cost installation, globally. The KNX system reacts quickly and deals intelligently in case of emergencies, with the presence or not of the owner. To implement our application, we proposed and realized the network topology shown in Figure 7.

Figure 7: Network Interconnection IP/KNX

We investigated the IP frames transmitted when detection of a gesture occurs in the smart home. The installation of KNX elements is done through the Engineering Tool Software (ETS). The interface between the IP (Ethernet or Wi-Fi) and KNX networks is provided with the IP/KNX hardware gateway.

The gesture recognition setting (1 or 2 hands raised for 3 seconds, for our example) allows to send HTTP requests to a server in order to control the switching of a lamp connected to a KNX module. On the same web server also runs a daemon called EIBd (European Installation Bus Daemon). It is software that interfaces the smart home and the KNX network. The presence of a reactive audio server to these requests also allows controlling a voice synthesizer which confirms the detected gestures and the triggering of corresponded actions.

5.3 Expanding the monitoring areas

For a better detection, we can use many Kinect sensors in the same room to expand the monitored area. Therefore, we are interested in linking multiple sensors in order to confirm an alarm detection. Indeed, if we suppose that we have three sensors in the same room, the event will be communicated through the network only if at least two sensors confirm the detection. The data redundancy avoids false detections. In a future work, we will use the IVY bus [29] for data communication between the sensors. It's a light software bus easy to handle in order to connect simple interactive applications written with different languages and running on different machines or platforms [30].

6 Conclusion

To continuously control their health, it is necessary to monitor dependent persons especially from afar. Taking care for people with reduced mobility is a part of medicine still in development. An automatic monitoring system seems to be interesting in the medical side. In this paper, we have proposed a solution to assist people using Kinect video sensors. We made a program which detects people gestures, recognize it and communicate it via a network to actuators. We should notice that the Kinect is not intrusive because, it does not film the person details but only her skeleton defined by 20 joints points. In a future work, we will implement an "Unistroke recognizer" [20] to use with Kinect. The main purpose is to implement more gestures to command the smart house using the appropriate algorithm. In prospect, we are currently working on fall detection using a performed 3D bounding box algorithm, to detect elderly falls. The system will be able to react in case of emergency by investigating the patient inactivity and sending alarms to a call center.

REFERENCES

[1] Emploi et Développement social Canada, http://www4.rhdcc.gc.ca/, 2014

[2] INSEE, Institut Nationale de la Statistiques et des Etudes Economiques, 2013

[3] Munro Dan, *The Year In Healthcare Charts, 2012*

[4] Dubert H. and Dormont B., *Vieillissement de la population et croissance des dépenses de santé* Report for the Montparnasse institut*, 2012*

[5] Wolf C., *Maintaining older people at home: Scientific Issues and technologies related tocomputer vision*,Etia 2011

[6] Conati C., Chabbal R. and Maclaren H., *A Study on Using Biometric Sensors for Monitoring User Emotions in Educational Games*, Department of Computer Science, University of British Columbia 2366 Main Mall Vancouver, BC, V6T 1Z4, Canada, 2004

[7] BillotA., *tutored project, : wireless sensors in biometrics* , ISIFC, 2007-2008

[8] http://www.senioractu.com/Loiret-Lysbox-un-boitier-connecte-pour-veiller-sur-les-personnes-agees_a17158.html, 2014

[9] Carner P., *Project Domus: Designing Effective Smart Home Systems*

[10] http://projects.laas.fr/HOMECARE/, 2014-2016

[11] Yohann Charlon, phdthesis, *conception d'un dispositif électronique pour l'aide au maintien des personnes âgées* , LAASLaboratory, 2014

[12] *The Guardian Angel Project*, Fet Flagship Pilot, Final report, public version, Federal PolytechniqueSchool of Lausanne, ETH Zurich (Switzerland), April 2012

[13] http://www.industrie-techno.com/guardian-angels-un-projet-europeen-sur-les-capteurs-du-futur.12667, 2012

[14] TölgyessyM., HubinskýP.,*The Kinect Sensor in Robotics Education*, Institute of Control and Industrial Informatics, Faculty of Electrical Engineering and Information Technology, Slovak University of Technology in Bratislava Slovakia, 2010

[15] http://mi.iut-blagnac.fr/

[16] PlyerA., *Visual perception and motion estimation*, ONERA-DTIM, Paris University 13, Thesis days 2011

[17] KerthoveT., *What is the difference between Kinect for Windows & Kinect for Xbox360*, Response of Microsoft to theUK independent review of intellectual property and growth, 4 March 2011.

[18] Anderson D., Bailey C.andSkubicM., *Hidden Markov Model symbol recognition for sketch-based interfaces*,AAAI Fall Symposium. Menlo Park, CA: AAAI Press, 15-21, (2004)

[19] SezginT.M and DavisR., *HMM-based efficient sketch recognition*, Proc. IUI '05. New York: ACM Press, 281-283(2005)

[20] WobbrockJ. O., WilsonA .D .andLiY., *Gestures without Libraries, Toolkits or Training: A $1 Recognizer for User Interface Prototypes*, University of Washington, UIST'07, October 7-10, 2007, Newport, Rhode Island, USA. ACM 978-1-59593-679-2/07/0010, 2007

[21] http://depts.washington.edu/aimgroup/proj/dollar/

[22] KristenssonP., NicholsonT. and QuigleyA., *Continuous Recognition of One-Handed and Two-Handed Gestures using 3D Full-Body Motion Tracking Sensors*, School of Computer Science University of StAndrews, St Andrews, United Kingdom, IUI'12, February 14-17, 2012,

[23] http://channel9.msdn.com/coding4fun/kinect/ Gestures-and-Tools-for-Kinect-and-matching-Toolkit-too-

[24] http://www.knx.fr

[25] Ben Hadj MohamedA., ValT., AndrieuxL. and KachouriA., *Using a Kinect WSN for home monitoring : principle, network and application evaluation*, ICWCUCA's, IEEE International Conference on Wireless Communications in Unusual and Confined Areas, Clermont-Ferrand, France, August 2012.

[26] YLi F., VandoniL., Zicca G. and ZanoliS., *OLSR Mesh Networks for Broadband Access: Enhancements, Implementation and Deployment*, 4th IEEE International Conference on In Circuits and Systems for Communications, ICCSC 200

[27] Joseph CampD. and Edward KnightlyW., *The IEEE 802.11s Extended Service Set Mesh Networking Standard*, Electrical and computer Engineering, rice University, Houston TX, 2006

[28] HirofuchiT., KawaiE., Fujikawa K. and H. Sunahara, *USB/IP - a Peripheral Bus Extension for Device Sharing over IP Netwo*, Nara Institute odf Science and Technology, 8916-5 Takayama, Ikoma, 630-0192, Japan, 2005 USENIX Annual Technical Conference

[29] http://www.eei.cena.fr/products/ivy/

[30] Réau. T, 2A2M training report, « Étude et développement d'un dispositif d'interaction multimodale pour l'aide et assistance à domicile », 2014

SOCIETY FOR SCIENCE AND EDUCATION UNITED KINGDOM

JBEMi JOURNAL OF BIOMEDICAL ENGINEERING AND MEDICAL IMAGING

ISSN: 2055-1266
VOLUME 1, ISSUE 6

Spatial Temporal based Classification for Antebrachium and Carpus Movement of EEG Data using Emotive Head Set

Muhammad Ahsan Gull[1], Javaid Iqbal[2] and Mohsin I. Tiwana
National University of Sciences & Technology, Islamabad, Pakistan.
[1]ahsangul74@mts.ceme.edu.pk; [2]j.iqbal@ceme.nust.edu.pk

ABSTRACT

Electroencephalographic (EEG) signals from test subjects are used for BCI analysis and classification of the four upper limb movements. Brain computer interface (BCI) system provides better neural control to the user, over two antebrachium and two carpus movement. This paper uses Epoc Emotiv head set with fourteen electrodes to acquire signal from the motor area of scalp. A particular protocol for data acquisition is followed. Our method is based on the time domain feature extraction techniques. Activity feature is applied on the signals. In order to discriminate between four upper limb movements within the data set, the paper uses Quadratic support vector machine, RBF SVM and Multilayer perceptron. The best classification accuracy of two antebrachium and two carpus movement is achieved by Quadratic SVM and RBF SVM when Gaussian window is used to calculate the activity feature vector. The number of correctly classified instants in term of percentage is 76.92% and 75.96% for quadratic SVM and RBF SVM. Current classifiers show promising results, where as to make conclusion more generalized and to enhance the classification accuracy, further experiments need to be carried out.

Keywords: Classification, Multilayer perceptron, Support Vector Machine, Hjorth Parameters.

1 Introduction

Brain Computer Interface provides us with a communication facility to actuate device using electroencephalographic signals. Currently, BCI is used to deliver commands to the processor, which transforms commands into certain specified actions. It's an emerging, fast-growing technology and is being used now a day for numerous controlling purposes. In this paper, experimental setup uses emotive headset for the collection of EEG data [8]. The main advantage of using emotive headset is that it is not only a noninvasive BCI technique to collect EEG data, but also provides better portability with fourteen active electrodes. A clinical survey showed that most of the causalities or strokes results in the disability of the people. Such a type of disability can be addressed either by restoring motor function of patients, or by providing them a prosthetic device [1]. Currently, evoked potential in combining with the

Data acquisition and offline analysis are supported by Department of Mechatronics Engineering (College of Electrical & Mechanical Engineering) National University of Sciences & Technology Pakistan. The research is carried out under the supervision of Javaid Iqbal and Mohsin I. Tiwana. This publication only reflects the author s' views.

DOI: 10.14738/jbemi.16.813
Publication Date: 5st January 2015
URL: http://dx.doi.org/10.14738/jbemi.16.813

robotic feedback is a sound technique to address the motor disability of the people [1]. Most important and recent research applications of BCI are controlling smart home appliances [2], wheel chair control, mobile robot control, controlling a prosthetic robotic arm, etc. [3] – [7].

This paper will classify the offline EEG data for two carpus and two antebrachium movements. Extensive literature review is carried out to classify upper limb movement from EEG data using different protocols and experimental setups. Table 1 shows brief survey of classification and feature extraction techniques which have been used to classify the different upper limb movements.

Table 1: Literature Review

References	*Classifiers*	*Feature*	*%age Accuracy*
G. N. Garcia T. Ebrahimi J.-M. Vesin [9]	Gaussian Support vector machine	Correlative time frequency based feature	86.00%
	Linear Discernment Analysis		61.00%
S. Solhjoo M. H. Moradi [10]	Gaussian Classifier	Power Spectral Density	65.4%
	Linear Discriminants Analysis		65.6%
	Bayes Quadratic		63.4%
	Mahalanobis distance		63.3%
H. Lee S. Choi, [11]	Support vector Machine + HMM	Principal Component Analysis	78.15%
	Hidden Markov Model		75.70%
Weibo Yi Shuang Qiu Hongzhi Qi Lixin Zhang Baikun Wan Dong Ming, [12]	Support vector machine	Multi-CSP	70.07%
		Multi-GECSP	68.73%
		Multi-sTRCSP	70.43%
Ricardo C.Caracillo Maria Claudia F. Castro, [13]	Linear Discriminant Analysis	Power Spectral Density	83.69% (Hand v/s arm) 67.95% (Right v/s Left limb)
J. Sleight P. Pillai S. Mohan, [14]	Support Vector Machine	Power Spectral Feature in Alpha beta & theta band	64.00%

This paper focuses on the noninvasive BCI technique, in which the EEG data is collected from a test subject using Emotive head set equipped with fourteen active electrodes. Data is recorded for each particular action for eight seconds. Once the data is recorded, fourth order Butterworth filter is applied for removal of unwanted artifacts and noise from the data set. For further rejection of undesired artifacts and to make the data unique to achieve the better classification of carpus-up, carpus-down, antebrachium-up, and antebrachium-down movements, it is a better practice to use windowing on data set for processing. Further, this paper uses supervised learning classification techniques (the quadratic SVM, radial based SVM and Multi-layer perceptron) to classify four upper limb movements when activity

(hjorth feature) is used as a feature extraction technique. Figure 1 shows schematic diagram for the whole process.

2 Experimental Protocol and Data Acquisition

An experimental protocol has been design to acquire the data for offline analysis. Two right handed subjects (age 25 and 26) participates in the data acquisition experimentation. Both subjects are neurologically stable and physically healthy. The experimental protocol consists of four right handed tasks (antebrachium-upward movement, antebrachium-downward movement, carpus-upward movement and carpus-downward movement). The subjects are instructed to avoid any facial expression or eye flickering in order to avoid unwanted artifacts while performing the tasks. Thirty trials with 1051 samples in 8.29 seconds are recorded from each test subject. The data from each test subject is recorded in a single trial whereas initial data set for a particular move is separated by markers. Mode of protocol used was P300.

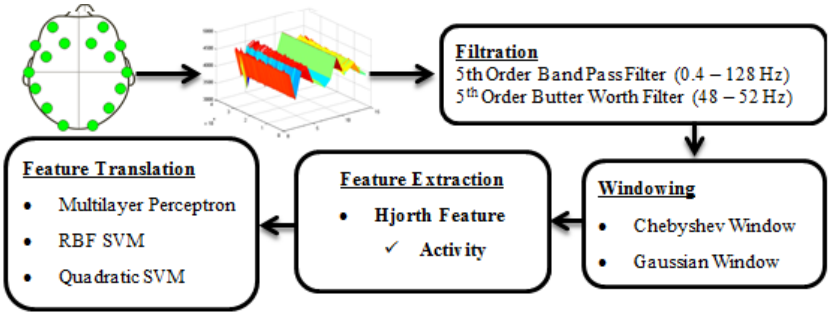

Figure 1: Schematic Diagram of Brain Computer Interface System

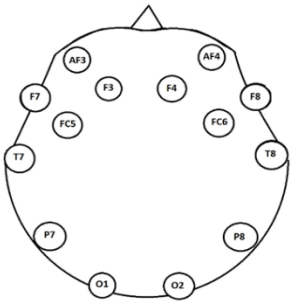

Figure 2: 14 Electrodes locations are shown

Emotiv Epoc neurohead set was used to acquire EEG data from the test subjects. These days, the research society uses EEG technology to classify and accomplish different tasks due to its prominent advantages over other technology as discussed in the Table 2.

Table 2: Brain sensing technologies and their primary disadvantages in BCI research

Technology	Primary Disadvantage
Electrocorticogram (ECoG)	Highly invasive, surgery
Magneto-encephalography (MEG)	Extremely expensive
Computed Tomography (CT)	Only anatomical data
Single Photon Emission Computerized Tomography (SPECT)	Radiation exposure
Positron Emission Tomography (PET)	Radiation exposure
Magnetic Resonance Imaging (MRI)	Only anatomical data
Functional Magnetic Resonance Imaging (fMRI)	Extremely expensive
Event-Related Optical Signal / Functional Near-Infrared (EROS/fNIR)	Still in infancy, currently expensive

By using Emotiv headset, data is recorded as per designed protocol. This EEG headset is equipped with 14 active electrodes use to acquire evoked potential from scalp. The sequential sampling rate of data is 2048 Hz and then the device down sample the data at 128Hz. Finally, the incoming data is filtered by fifth order sinc notch filter. Table 3 discusses the necessary specifications of Emotiv headset and figure 2 shows the location of 14 sensors over scalp.

Table 3: EMOTIV EPOC Neuro headset Specification [8]

No. of Channels	14 (plus CMS/DRL references, P3/P4 locations)
Channels Name	AF3, AF4, F3, F4, F7, F8, FC5, FC6, P7, P8, T7, T8, O1, O2.
Sampling Rate	~128Hz
Sampling method	Sequential sampling. Single ADC
Resolution	14 bits 1 LSB = 0.51µV (16 bit ADC, 2 bits instrumental noise floor discarded)
Filtering	Built in digital 5th order Sinc filter
Dynamic range	8400µV (pp)
Coupling mode	AC coupled
Connectivity	Proprietary wireless, 2.4GHz band
Power	LiPoly batteries
Battery life	12 hours

3 Filtration and Windowing

Once the data is acquired, it is band pass filtered (0.4-128 Hz) with 500 Hz sampling frequency and fifth order butter worth filter (48Hz – 52Hz) is used to clip the baseline noise. In BCI, the aim of filtration is to remove the unwanted artifacts recorded during data acquisition [13]. After filtration, a better practice to extract the feature is to make a window on the data set. The size of window should be carefully selected because larger window can accommodate outlier while calculating the feature and much smaller

window can lose confidence. In this paper, the window applied on the data set is of 52X1 with 0.1 sec step size [13]. Two different types of windows (Gaussian window and Chebyshev window) were applied on the data set for analysis as shown in the figure 3.

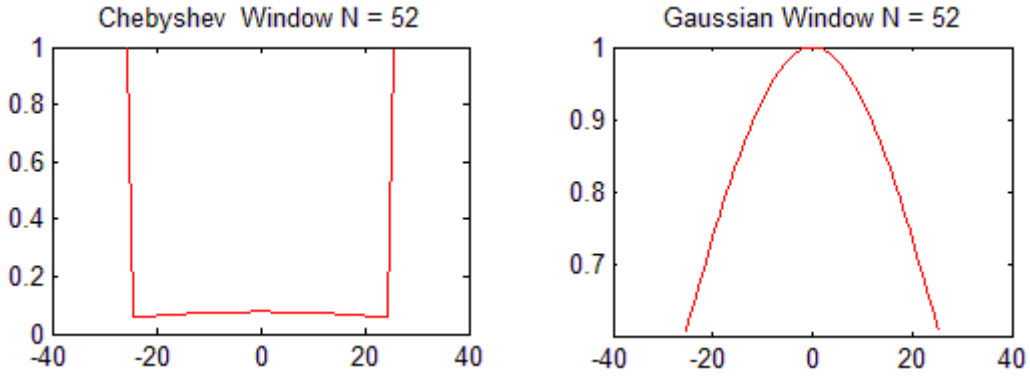

Figure 3: Gaussian window of N = 52 samples and alpha = 1. Here alpha is inversely proportional to Standard deviation. And Chebyshev window of 52 samples with side lobe magnitude r = 9

4 Feature Translation

A Time domain feature extraction technique, Activity (also known as one of the hjorth features) is used for the reduction of artifacts. Different artifacts removal techniques are used by various authors as mentioned in the Table no. 1. In BCI, the aim of feature extraction is to remove the unwanted artifacts recorded during data acquisition [10] like eye blinking, other unwanted muscular activity and etc.

$$y(x_i) = \sqrt{\frac{var\,(x_i')}{var\,(x_i)}} \tag{1}$$

x_i represents the signal, x_i' is the rate of change of signals and $y(x_i)$ is the measure of signal's mean frequency. A hjorth approach, activity is also used in this paper to find the attributes. Mathematically it can be represented as.

$$Activity(x) = \frac{\sum_{n=1}^{n}(x_n - \bar{x})^2}{N} \tag{2}$$

X_n is nth number of sample in the data set and is the mean and N be the total number of samples. Activity calculates that how much signal is deviated from its mean value. The topographical distribution of feature vector is shown in the figure4. There are different frequency domain methods for calculating the feature vector like PSD, BP, wavelet, Fourier, AR and etc. but they have complex parameters and causes to enhance over fitting difficulties while classifying dat.

5 Classification Techniques

Once feature vector have calculated now classify the data depending upon the feature. This paper used one against one technique for RBF support vector machine and quadratic SVM to classify the four upper limb movements by constructing a nonlinear hyper plane in feature space. Mathematically support vector machine is represented by following equation.

$$c = \sum_i a_i k(s_i, x) + b \tag{3}$$

s_i is support vector, a_i is weight and ***b*** is the bias that is used to classify the feature vector ***x***. Here ***k*** is the kernel function. Two types of kernel functions are used in this paper radial based kernel and quadratic kernel to separate the data. Equation 5 and 6 shows the mathematical representation of radial based function and quadratic function respectively.

$$k(s_i.x) = e^{-\|s_i - x\|^2} \tag{4}$$

$$k(s_i.x) = (s_i.x + r)^2 \quad \text{Where} \quad r \geq 0 \tag{5}$$

r is the quadratic function parameter needed to be selected carefully for better classification. The classification accuracy of upper limb movement using support vector machine is shown in [12] and [14]. While [11] uses cascading of SVM with hidden markov model to classify the forearm movement. Another paradigm used to classify the two antebrachium and two carpus movement used in this paper is multi-layer perceptron. Its formulation is as follows.

$$y = f(a)(\sum_{i=1}^{k}(w_i x_i + d)) \tag{6}$$

f(a) is the activation function, ***d*** is the bias, ***w*** is the weight and ***x*** is the feature vector. Using BCI competition IV, A dataset for three motor imageries (left hand, right hand and right foot), multilayer perceptron shows 85.71% classification accuracy with 0.1 learning rate [16].

6 Results and Discussion

The overall classification rates of above mentioned classifier with activity as a feature are shown in the table 4. Based on the literature survey, analysis, and results obtained, it can be concluded that Quadratic support vector machine and radial based function support vector machine give the best classification accuracy of 76.92% and 75.96% when Gaussian window of 0.1 millisecond is used to find the activity feature vector. The analysis of Quadratic support vector machine and RBF SVM for the classification of four upper limb movement using activity (hjorth feature) presented in this paper is novel. Whereas better classification of antebrachium downward movement, antebrachium upward movement, Carpus downward movement and carpus upward movement is 92.31%, 80.70%, 63.00% and 80.70%, respectively, using activity with quadratic SVM. RBF SVM and quadratic SVM with activity feature shows much better results (shown in the table4) as compared to the SVM with principal component analysis, power spectral density, Multi-CSP Multi GECSP and Multi-sTRCSP used as the feature extraction techniques. whereas literature survey reports the classification accuracy of upper limb movement using SVM with principal component analysis [11], power spectral density [14], Multi-CSP [12], Multi GECSP [12] and Multi-sTRCSP [12] is 78.15%, 64.00%, 70.07%, 68.73% and 70.43% respectively. Table 4 expresses the classification accuracy of three classifiers. Best classification accuracy of multilayer perceptron is 72.06% when Gaussian window is used for calculating activity feature vector. By applying Chebyshev window it is found that MLP shows 70.43% correctly classified instants. Figure 4 shows the topographical distribution of four upper limb movements. In figure 4 the red area shows convergence of the data over the left hemisphere of frontal lobe of motor cortex, the maps are made based on the activity (hjorth value) values of each electrode.

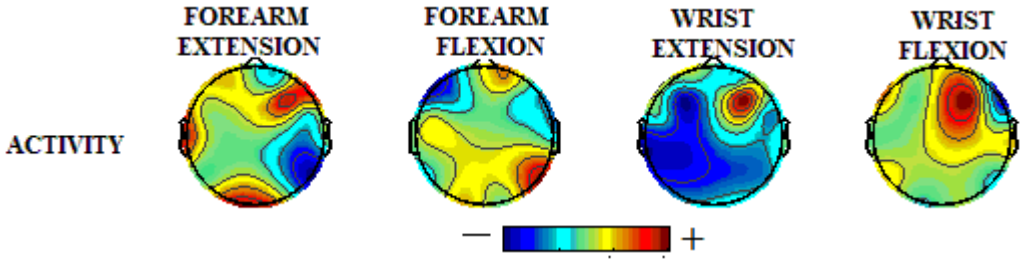

Figure 4: Topoplots of feature vector (Activity) for Brachium Down movement, Brachium Up movement, Carpus Down movement and Carpus up movement

Table 5 shows stratified cross validation results and weighted average accuracy of multilayer perceptron. These results shows some deviation and this may be due to the reason that if the size of classes differs it causes misclassification and the number of false positives increases .This research has great importance, due to the reason that one can understand that how specific neural activity is differ from the other motor area. In order to enhance true positive and make the solution more generic it is necessary to increase number of trials by increasing number of test subjects.

Table 4: Percentage Accuracy of Classifier with Activity feature for four upper limb movement.

Classification Algorithm	Gaussian Window	Chebyshev Window
Quadratic SVM	76.92%	73.08%
RBF SVM	75.96%	72.52%
MLP	72.60%	70.43%

Table 5: Stratified cross validation results and weighted average accuracy by class.

Multilayer Perceptron (MLP)	Kappa Statistic	Mean Absolute Error	Relative Absolute Error	Coverage of Class (0.95 level)	Mean rel. Region Size (0.95 level)	False Positive (Weighted Avg.)	True Positive (Weighted Avg.)
Gaussian Window	0.6346	0.168	44.80%	95.67%	50.18%	0.726	0.091
Chebyshev Window	0.6058	0.1724	45.97%	93.02%	47.59%	0.704	0.099

7 Conclusion

The current BCI research is focused on the optimization of classifier algorithms and better neural plasticity. In this study, the performance of Quadratic support vector machine, RBF support vector machine and Multilayer Perceptron using activity feature for the optimized classification of antebrachium upward-movement, antebrachium-downward movement, carpus-downward movement and carpus-upward movement has been investigated and analyzed. In this analysis, the best results achieved by Quadratic SVM and RBF SVM classifiers are 76.92% and 75.96% when activity is used as feature. Future work is aimed at enhancing the performance of algorithm to attain better classification results and to make the solution more generic by enhancing the number of data samples and number of test subjects.

REFERENCES

[1]. Kai Keng Ang; Cuntai Guan; Kok Soon Phua; Chuanchu Wang, Irvin; The Chang Wu Chen; Effie Chew:" Transcranial direct current stimulation and EEG-based motor imagery BCI for upper limb stroke rehabilitation" 34th Annual International Conference of the IEEE EMBS San Diego, California USA, 28 August - 1 September, 2012.

[2]. Wei Tuck Lee; Humaira Nisar; Aamir S. Malik; Kim Ho Yeap, "A Brain Computer Interface for Smart Home Control" 2013 IEEE 17th International Symposium on Consumer Electronics (ISCE)

[3]. L. R. Hochberg; M. D. Serruya; G. M. Friehs; J. A. Mukan; M. Saleh,A. H. Caplan; A. Branner; D. Chen; R. D. Penn; and J. P. Donoghue. "Neuronal ensemble control of prosthetic devices by a human with tetraplegia." Nature, vol. 442, no. 13, pp. 164–171, Jul. 2006

[4]. S. M. T. Müller; W. C. Celeste; T. F. Bastos-Filho; and M. Sarcinelli- Filho. "Brain-computer Interface Based on Visual Computer Interface Based on Visual Evoked Potentials to Command Autonomous Robotic Wheelchair." Journal of Medical and Biological Engineering, vol. 30, no. 6, pp. 407–416, 2010.

[5]. Birbaumer N; Ghanayim N; Hinterberger T; Iversen I, Kotchoubey B, Ku ¨bler A, Perelmouter J, Taub E, Flor H. "A spelling device for the paralyzed". Nature 398:297–298. doi:10.1038/18581, 1999.

[6]. M. Asghari Oskoei and H. Hu. "Support vector machine-based classification scheme for myoelectric control applied to upper limb" IEEE Transactions on Biomedical Engineering, vol. 55, no. 8, pp. 1956-1965, 2008.

[7]. Wolpaw JR; Birbaumer N; McFarland DJ; Pfurtscheller G; Vaughan TM. "Brain–computer interfaces for communication and control." Clin Neurophysiol 113:767–791. doi: 10.1016/S1388-2457(02)00057-3, 2002.

[8]. Emotiv.com (2013). EPOC Features. [online] Retrieved from: http://www.emotiv.com/epoc/ [Accessed: 5 Mar 2013].

[9]. G. N. Garcia; T. Ebrahimi and J.-M. Vesin. "Support vector EEG classication in the Fourier and time-frequency correlation domains." In Conference Proceedings of the First International IEEE EMBS Conference on Neural Engineering, 2003.

[10]. S. Solhjoo and M. H. Moradi. "Mental task recognition: A comparison between some of classication methods." In BIOSIGNAL 2004 International EURASIP Conference, 2004

[11]. H. Lee and S. Choi. "Pca+hmm+svm for eeg pattern classification." In Proceedings of the Seventh International Symposium on Signal Processing and Its Applications, 2003.

[12]. Yi et al.: "EEG feature comparison and classification of simple and compound limb motor imagery." Journal of NeuroEngineering and Rehabilitation 2013 10:106.

[13]. Ricardo C.Caracillo and Maria Claudia F. Castro. "Classification of Executed Upper Limb Movements by Means of EEG." In Biosignals and Biorobotics Conference (BRC), 2013 ISSNIP.

[14]. J. Sleight, P. Pillai, and S. Mohan, "Classification of Executed and Imagined Motor Movement EEG Signals," Ann Arbor, p. 10, 2009.

[15]. Johnny Lee and Desney Tan. "Using a low-cost electroencephalograph for task classification in hci research." UIST'06: Proceedings of the 19th annual ACM symposium on User interface software and technology, Oct 2006.

[16]. G.V. Sridhar and Dr. P. Mallikarjuna Rao "A Neural Network Approach for EEG classification in BCI." International Journal of Computer Science and Telecommunications [Volume 3, Issue 10, October 2012]